Nanoscale

COMMUNICATION

View Article Online
View Journal

Check for updates

Cite this: DOI: 10.1039/d5nr01472g

Received 11th April 2025,
Accepted 14th July 2025

DOI: 10.1039/d5nr01472g

rsc.li/nanoscale

Published on 06 Agosti 2025. Downloaded on 03/10/2025 02:20:03.

Non-invasive imaging-guided preclinical assessments reveal high performance photothermal effect of an Au-solid lipid nanomaterial

Chetna Patnaik, [a,b] B. Pradeep K. Reddy, [c] Anuradha Gupta, [a,b] Sulagna Rath, [a,b] Suditi Neekhra, [c] Sabyasachi Chakrabarty,[c] Pradip Chaudhari,[d] Shahzada Asad,[e] Arvind Ingle, [d] Rohit Srivastava *[c] and Abhijit De *[a,b]

With the rising global cancer crisis, photothermal therapy (PTT) has emerged as a promising treatment for solid tumours. PTT utilizes near-infrared (NIR) photons to generate localized heat through plasmonic nanoparticles. We optimized the production of a novel PTT nanomaterial, a gold-coated solid lipid nanoparticle (Au-SLN), and characterized its functionalities using non-invasive multimodality imaging. Synthesized *via* solvent-emulsion evaporation, Au-SLNs achieved 80% photothermal conversion efficiency, surpassing that of many existing agents. The lyophilized product demonstrated high reproducibility, biocompatibility, cell permeability, and non-toxicity, which are essential for clinical translation. To evaluate *in vivo* hyperthermic potential, infrared thermography (IRT), bioluminescence imaging (BLI), NIR fluorescence (NIRF), and microCT imaging were employed using an orthotopic murine breast cancer model. IRT confirmed significant thermal elevation ($p < 0.0001$), while tomographic imaging modalities provided comprehensive insights into the primary debulking efficiency and post-treatment healing process. PTT using Au-SLNs resulted in complete remission of small tumours, but for late-stage tumours, booster dose optimization was required to deliver enhanced survival benefits. These findings underscore the therapeutic potential of Au-SLNs as an effective standalone photothermal agent for treating solid tumours. This study shows that PTT-mediated tumour debulking greatly improves post-treatment life expectancy with no visible distress symptoms, thus paving the way for its future clinical application.

Introduction

One of the pressing issues in public health is the astounding incidence of global cancer-related deaths. In 2022, an estimated 20 million new cancer cases and 9.7 million cancer-related deaths occurred globally. The likelihood of developing cancer in one's lifetime is about 1 in 5, with approximately 1 in 9 men and 1 in 12 women succumbing to the disease.[1,2] Surgery, chemotherapy, and radiotherapy are the standard of care in cancer clinics, but patient deaths due to relapse are still significant. With the high risk of treatment-related toxicity, the chance of invariable disease relapse, metastatic spread and compromised living experience post-therapy in many aggressive types or subtypes of cancers, the global cancer burden status and healthcare costs have emerged as a great concern.[2] Many newer and precise forms of therapeutic avenues utilizing immune cells and versatile nanotherapeutics have emerged through research as promising approaches, showing their ability to improve survival in relapse and recurrent cancer cases.[3,4] The original concept of hyperthermic cancer treatment was documented by Hippocrates, who suggested that a tumour cannot be surgically excised and that it should be thermally treated.[5] Thermal therapy involves elevating the core temperature of a tumour, thereby inducing irreversible damage to the DNA and protein contents of tumour cells.[6] Selective or regional hyperthermia applications have shown efficacy in achieving complete cell ablation, irrespective of the cancer type or aggressiveness.[7] Importantly, this physical treatment procedure represents a limited risk of developing resistance against the treatment procedure.

In this context, photothermal therapy (PTT) is particularly promising as it utilizes plasmonic nanoparticles engineered to generate local heat when triggered by near infrared (NIR) photons. Once these nanoparticles accumulate in the vicinity of tumour tissues and are exposed to NIR photons, heat is generated due to the oscillation of free electrons, a phenomenon known as surface plasmon resonance (SPR).[8] This same effect

[a]*Molecular Functional Imaging Lab, Advanced Centre for Treatment, Research and Education in Cancer (ACTREC), Tata Memorial Centre, Kharghar, Navi Mumbai-410210, India. E-mail: ade@actrec.gov.in*
[b]*Department of Life Sciences, Homi Bhabha National Institute, Mumbai-400094, India*
[c]*Department of Biosciences and Bioengineering (BSBE), Indian Institute of Technology Bombay, Powai, Mumbai-400076, India. E-mail: rsrivasta@iitb.ac.in*
[d]*Laboratory Animal Facility, Advanced Centre for Treatment, Research and Education in Cancer (ACTREC), Tata Memorial Centre, Kharghar, Navi Mumbai-410210, India*
[e]*Revvity Healthcare, Ghodbunder Road, Thane West-400615, India*

Published on 06 Agosti 2025. Downloaded on 03/10/2025 02:20:03.

does not apply in the neighbouring tissue environment where either the material or photonic exposure is lacking.[9] The effectiveness of PTT in cancer hinges on two critical factors: first, the precise localization of nanoparticles within the target area, and second, the activation by the NIR photon beam within the target region.[10] Various gold nanomaterials have been used for PTT owing to the biologically inert property of gold and thereby its systemic biocompatibility, tuneable shape and size, as well as ease of surface functional modifications.[11] Preclinical trials using gold-based PTT monotherapy in larger animals, such as canines and felines, have been attempted, showing promising therapy efficacy in treated solid tumours. A notable example would be the use of gold nanorod-mediated PTT for mammary tumours in dogs and cats, demonstrating no toxicity in vital parameters and overall survival improvement to 315.5 ± 20.5 days.[12] Human clinical trials were also performed utilizing photothermal gold-silica nanoshells (AuroshellTM) in prostate cancer patients, demonstrating the safety and technical feasibility of employing PTT in clinical settings.[13] Additionally, in recent years, various multifunctional PTT nanomaterials have been developed by combining PTT with other standardized therapy applications.[8,14–16] Although this multi-prong treatment approach could overcome suboptimal PTT effect, a multifunctional material may complicate clinical trial entry in terms of receiving regulatory approval and/or their scale-up production scope.

Against this backdrop, here, we synthesize a novel nanomaterial for PTT, *i.e.* gold-coated solid lipid nanoparticle (Au-SLN), using glyceryl palmitostearate and stearyl amine to form the solid lipid core of the nanoformulation. The material was rigorously tested for reproducible production, scale up ability, physical characterization, and material biocompatibility. Comprehensive assessments of *in vivo* biodistribution, toxicity and body clearance were performed. Photothermal efficacy and survival benefit measurements were estimated using comprehensive non-invasive multimodality imaging applications in an orthotopic breast cancer mouse model.

Results and discussion

Synthesis and physical characterization of Au-SLN show favourable properties for biomedical applications

The solvent emulsion evaporation method was employed for the synthesis of solid lipid nanoparticles (SLN) (Fig. 1a). After organic solvent evaporation, the visible conversion of the milky white turbid emulsion to a transparent solution provided preliminary assurance of efficient SLN synthesis. The gold coating of SLN was achieved using ascorbic acid as a reducing agent, following the core–shell phenomenon.[17] With increasing gold shell thickness, product absorbance shifts towards the NIR window.[18,19] Across the batches of the prepared Au-SLN, the peak tuning at 750 nm was confirmed (Fig. 1b and Fig. S1a and b). The hydrodynamic diameter of the particles was 80 ± 10 nm (Fig. 1c), and the poly-dispersity index (PDI) was 20 ± 10%, as recorded by dynamic light scattering (DLS). A smaller population of particles was observed with a hydrodynamic diameter of less than 10 nm, which could be attributed to micellar components.[20] The zeta potential of SLN was 25 ± 2 mV, while the zeta potential of Au-SLN was −11 ± 2 mV, which were both compatible for biological applications.[21] The SLN thus obtained was observed using cryo-scanning electron microscopy (cryo-SEM) imaging to obtain a spherical morphology in the range of 60 ± 10 nm (Fig. S2). Transmission electron microscopy (TEM) and high-angle annular dark-field (HAADF) images revealed the irregular morphology of Au-SLN with a diameter in the range of 70 ± 15 nm (Fig. 1d and e). Additionally, high-resolution TEM (HRTEM) illustrated the unique lattice configuration of gold (Fig. 1f), with a spacing of approximately 2 Å (measured using Image J). Moreover, the X-ray diffraction rings showed corresponding (111), (200), (220), and (311) band reflections, indicating the characteristic face-centred cubic (fcc) crystalline structure of gold (Fig. 1g). Energy-dispersive X-ray (EDX) spectroscopy results confirmed the deposition of elemental gold over the SLN particles (Fig. 1h). ICP-AES analysis revealed a gold concentration of approximately 50 μg mL^{-1} in the batches of Au-SLN prepared (Table S1), and their recorded PTT profiles are tabulated in Table S2.

Au-SLN holds an efficient photothermal conversion and transduction efficiency

When the frequency of the incident electromagnetic radiation coincides with the resonant frequency of surface plasmons on gold nanoparticles, heat energy is transduced. The efficiency of photothermal conversion upon tuned NIR photon incidence on Au-SLN was calculated. Compared to water as a control, the Au-SLN temperature profile was generated after irradiation with 750 nm and 650 mW (*i.e.* 3.3 W cm^{-2} power density) laser until a steady state was reached (Fig. 2a and Fig. S3a). The time constant and heat transfer constant for heat transfer by Au-SLN were calculated by applying the natural logarithm of temperature change with respect to the surrounding *versus* time data obtained from the cooling cycle (Fig. 2b and Fig. S3b). Au-SLN showed an excellent photothermal conversion efficiency (PCE) of 80.27%, *i.e.*, approximately 80% of the incident NIR wavelength energy is converted to thermal energy by this product (Result S1). This is much higher than the photothermal agents previously reported by our group (Table 1).

As Au-SLN is a potent photothermal agent with 80.27% light to heat energy conversion efficiency, its clinical/preclinical administration must be carefully performed to minimize hyperthermic damage to neighbouring non-cancerous cells. Laser-irradiated Au-SLN produces sufficient localized heat that causes cellular ablation in the area; thus, an optimal experimental space has to be applied to prevent bystander heat damage. However, the optimal use of the duration of laser incidence is also important to achieve control over the heating effect on neighbouring tissues. With the help of the design of the experiment, the cumulative impact of photothermal material concentration, laser power and duration of laser incidence on the heat energy generated was evaluated using

 This journal is © The Royal Society of Chemistry 2025

Published on 06 Agosti 2025. Downloaded on 03/10/2025 02:20:03.

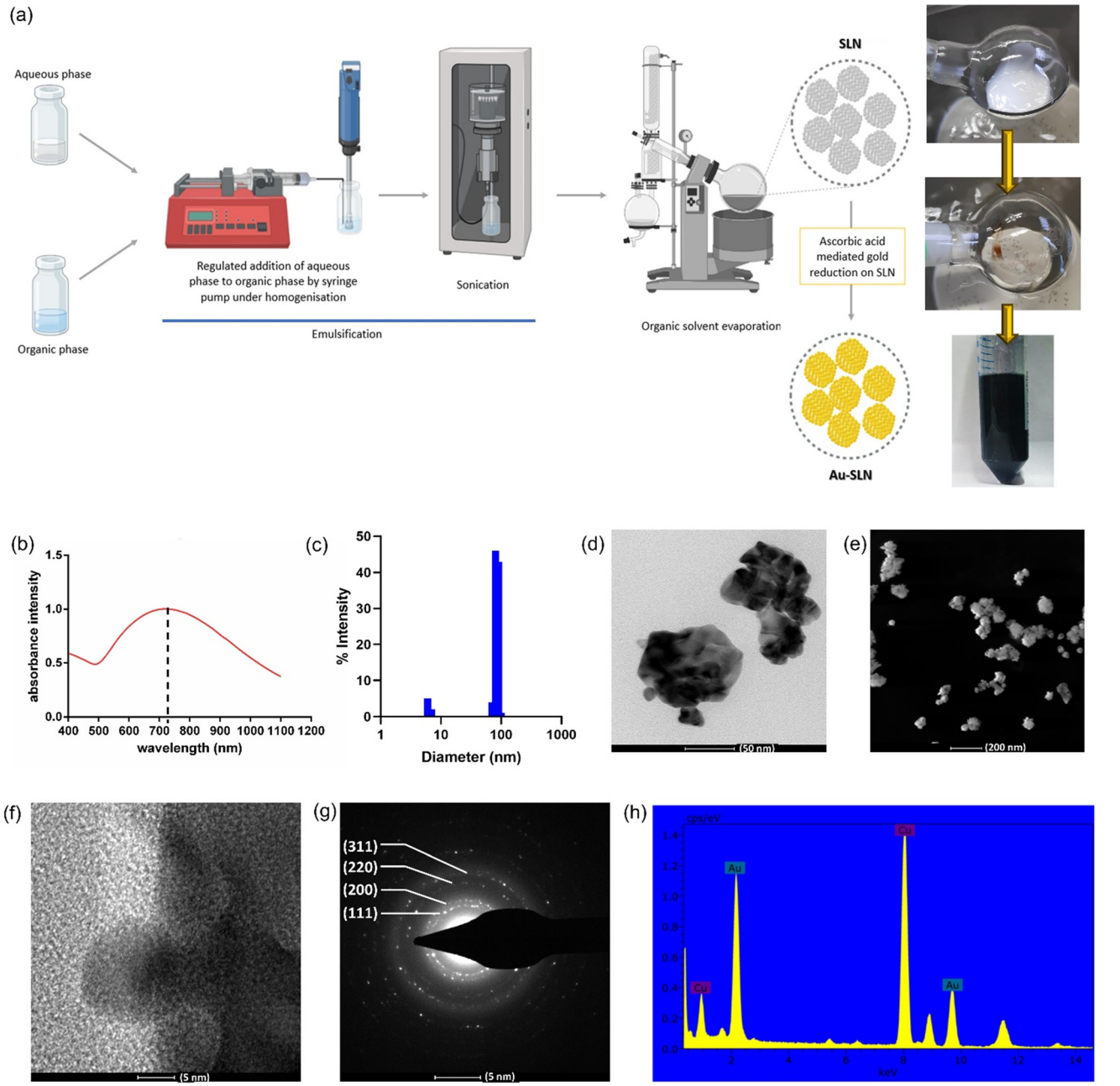

Fig. 1 Synthesis and physical characterization of Au-SLN. (a) Schematic representation of solvent emulsion evaporation process followed for Au-SLN synthesis; (b) UV-visible absorbance spectra showing peak tuning of Au-SLN; (c) hydrodynamic diameter assessment of Au-SLN by DLS; (d) TEM of Au-SLN, and the scale bar denotes 50 nm; (e) HAADF of Au-SLN, and the scale bar denotes 200 nm; (f) HR-TEM of Au-SLN, and the scale bar denotes 5 nm; (g) SAED of Au-SLN, and the scale bar denotes 5 nm; and (h) EDX spectroscopy of Au-SLN.

response surface methodology (RSM) (Fig. 2c). A face-centred central composite design (CCD) was constructed with 17 runs, and the corresponding experimental temperature response values (°C) were recorded (Table 2).

A quadratic model based on sequential sum of squares was chosen (Table S3). ANOVA analysis demonstrated that the model was statistically significant ($p < 0.05$), with the lack of fit being insignificant ($p > 0.05$) (Table S4). The *R*-squared value for the model was 0.9689. Additionally, the small difference (<0.2) between the adjusted *R*-squared (0.929) and predicted *R*-squared (0.7504) further supports the significance of the chosen model. The coded equation representing the quadratic model's depiction of variable effects on the response is presented in the following equation:

$$Y = +71.69 + 0.046A + 2.56B + 8.49C - 1.49AB - 1.61AC + 0.0875BC - 12.63A^2 + 0.5746B^2 - 8.28C^2,$$

Published on 06 Agosti 2025. Downloaded on 03/10/2025 02:20:03.

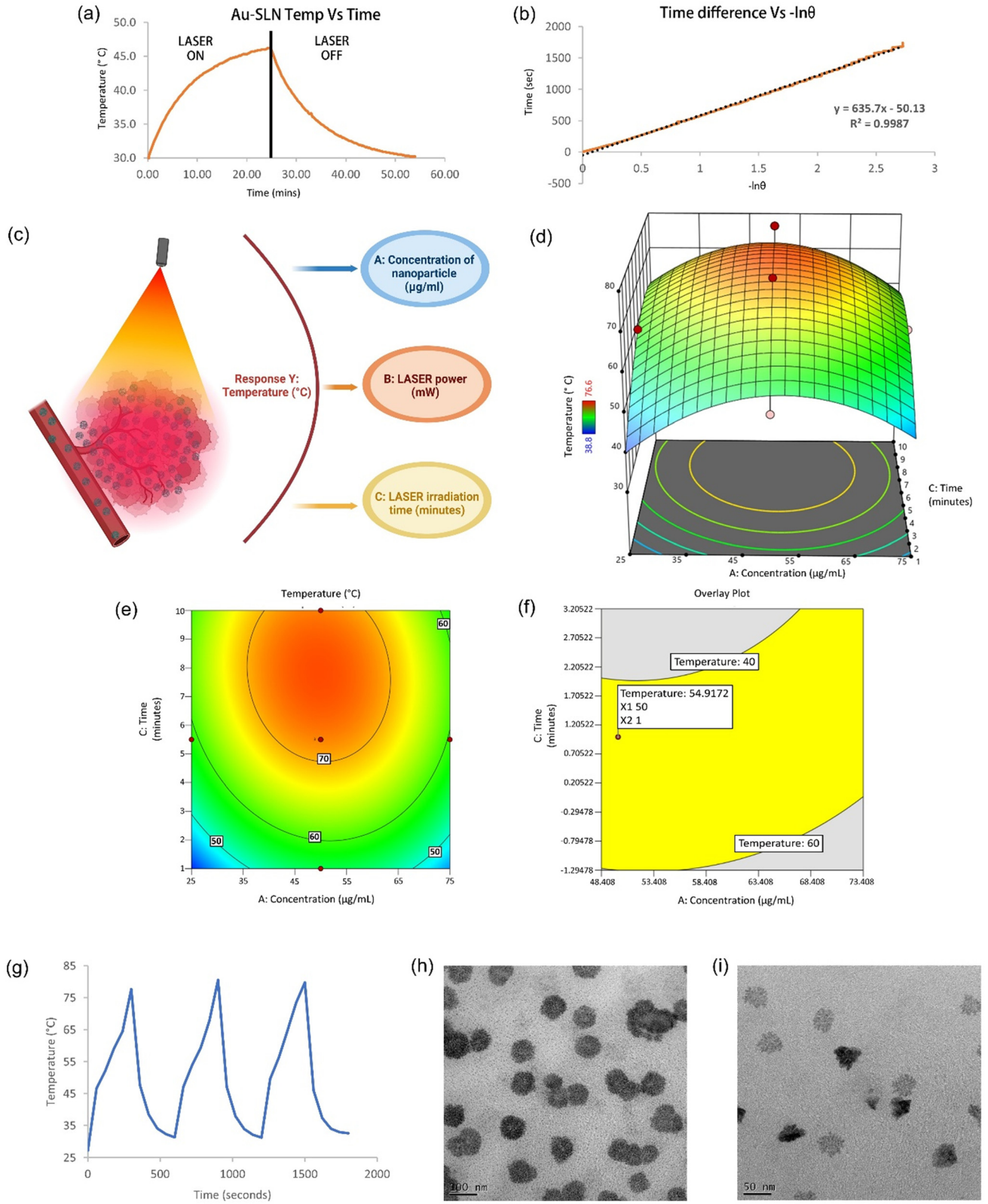

Fig. 2 Photothermal conversion and transduction potential of Au-SLN. (a) Temperature profile corresponding to NIR laser ON and OFF for Au-SLN; (b) time difference with respect to negative logarithm of temperature post laser OFF for Au-SLN; (c) impact of independent variables *A*, *B* and *C* on dependent variable/response, *i.e.*, temperature using DOE; (d) response surface 3D plot for the temperature response with respect to Au-SLN concentration and LASER irradiation time at a power density of 3.3 W cm^{-2}; and (e) contour graph of the temperature response; (f) design space of the optimized temperature overlay plot; (g) thermal stability analysis of Au-SLN over multiple cycles of PTT; (h) Au-SLN-TEM before NIR laser incidence; and (i) Au-SLN-TEM post three rounds of PTT; the scale bar denotes 50 nm.

 This journal is © The Royal Society of Chemistry 2025

Published on 06 Agosti 2025. Downloaded on 03/10/2025 02:20:03.

Table 1 PCE comparing Au-SLN with reported photothermal agents

Nanoformulation	PCE	Ref.
Au-SLN	80.27%	—
Tocophotoxil (750 nm)	25.6%	22
Tocophotoxil (915 nm)	20.8%	22
BF2-oxasmaragdyrin nanoparticles	43.6%	23
Peptide conjugated BF2-oxasmaragdyrin nanoassemblies	56.6%	24
CuS/ZnS nanocomposites	40.15%	25
Gold-zein nanoparticles	65.05%	26
Au-PNVCL nanoshells	63.17%	17
Plasmonic zein nanoshells	22.85%	27
GO-IR 780	22.75%	28
GO-AuPLGA	22.01%	28

Table 2 CCD design matrix with experimental results

Runs	Factor 1: *A* concentration of nanoparticle (μg mL^{-1})	Factor 2: *B* laser power (mW)	Factor 3: *C* laser irradiation time (minutes)	Response *Y*: temperature (°C)
1	25	650	5.5	58.9
2	25	750	10	63.9
3	75	650	5.5	59.2
4	75	750	10	57.9
5	50	650	5.5	69.9
6	75	750	1	47.2
7	25	550	10	55.6
8	75	550	1	45.2
9	25	550	1	38.8
10	50	650	10	76.6
11	50	650	1	50.2
12	50	550	5.5	68
13	25	750	1	45
14	50	750	5.5	76.5
15	50	650	5.5	72.6
16	50	650	5.5	72.6
17	75	550	10	57.3

where *A*, *B*, *C* and *Y* denote concentration of the nanoparticle in μg mL^{-1}, laser power in mW, laser irradiation time in minutes and temperature response (°C), respectively. It may be observed from the equation that *C* has a major synergistic impact on temperature response, followed by *B* and *A*. The effect of these factors on the resultant temperature can be observed using the response surface 3D plot and contour graph (Fig. 2d–f).

Furthermore, the design space was assessed by selecting three distinct points within it and comparing the observed values with the corresponding predicted values. As presented in Table 3, the experimental outcomes fell within the predicted ranges, confirming that the design space was successfully evaluated within a two-sided 95% confidence prediction interval. The quadratic model, developed using RSM, enables accurate temperature prediction for any tested nanoparticle concentration, laser power, and irradiation time. This precision is critical for PTT, where small temperature changes impact efficacy. The model streamlines parameter selection, minimizes experimental trials, and ensures safe and effective PTT by facilitating the *in silico* optimization of treatment conditions.

Besides the superior photothermal conversion efficiency, the stability of recoverable temperature over 3 consecutive laser-on/off cycles showed stable photothermal efficiency in all three cycles (Fig. 2g). Following repetitive PTT, the material was also analysed by TEM, which showed disintegrated particles (Fig. 2h and i). These results indicate that with a single administration of Au-SLN, repeated exposure with laser can be performed to deliver PTT boosters when required. Further, the disintegration of the material post-PTT facilitates efficient renal clearance.

Lyophilization of Au-SLN enhances its storage stability under economically viable conditions

As the Au-SLN formulation was optimized to ensure bulk production, another important industrial factor to optimize was the lyophilization or freeze-drying of Au-SLN. The colloidal state of Au-SLN was observed to be stable for up to a month, with little to no aggregate formation. However, to further enhance the shelf life of this nanomaterial, its lyophilization was optimized using sugars as traditional cryo- and lyo-protectant. The presence of sugars helps stabilize the morphology of the nanoformulation by immobilizing the nanoparticles in a matrix, thus preventing their aggregation as well as protecting them from the mechanical stress of freeze-drying imparted by ice crystal formation.[29,30] We used different concentrations of sugars, such as lactose, trehalose, sucrose, mannitol and stabilizing agent F-68, to assess the lyophilization efficiency (Table S5). For lyophilization optimization with 1% F-68 and 2.5% lactose, we observed good cake formation post lyophilization (Fig. 3a), which was readily reconstituted in Milli-Q in a minute. Their hydrodynamic diameter, polydispersity index and UV-visible absorbance intensity at 750 nm (Fig. 3b) were also observed to be comparable with freshly prepared stable Au-SLN and confirmed as cryoprotectants for future studies.

To establish the storage stability of the lyophilized nanoformulation, Au-SLN lyophilized using 1% F-68 and 2.5% lactose was stored under two conditions: a cold temperature of 4 °C and a room temperature of 25 °C at 55–60% relative humidity; these are the most economically feasible conditions for both storage and transportation. The stability assessment was per-

Table 3 Post analysis confirmation for validation of design space

Trial run	*A*	*B*	*C*	95% PI low temperature (°C)	Observed temperature (°C)	95% PI high temperature (°C)
1	50	650	2	52.02	54.2	68.88
2	50	650	3	56.16	58.8	72.5
3	50	650	4	60.0	63.4	76.2

Published on 06 Agosti 2025. Downloaded on 03/10/2025 02:20:03.

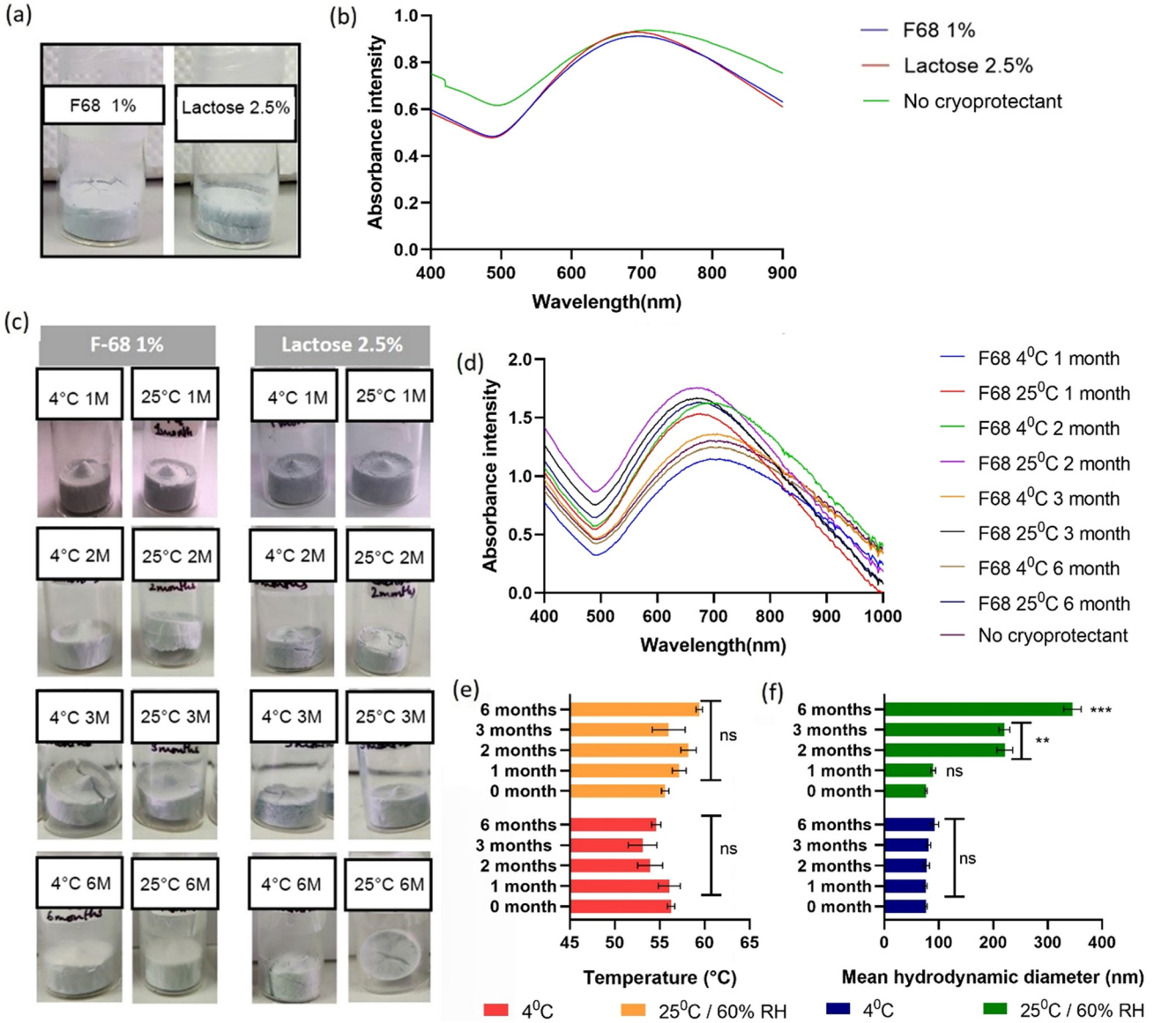

Fig. 3 Lyophilization and storage stability of Au-SLN. (a) Photograph of the final formulation of lyophilized cakes of Au-SLN using 1% F-68 and 2.5% lactose; (b) UV-visible absorbance spectra for NIR peak tuning of the final lyophilization formulations of Au-SLN using 1% F-68 and 2.5% lactose; (c) photograph of sample lyophilized products of Au-SLN using 1% F-68 and 2.5% lactose stored at 4 °C and 25 °C at 55–65% R.H. for 1, 2, 3, and 6 months post synthesis; (d) UV-Visible absorbance spectra to check peak absorbance following resuspension of lyophilized Au-SLN cakes in Milli-Q as a measure of product stability for up to 6 months using 1% F-68 as cryoprotectant; (e) photothermal conversion profile of 50 mg mL^{-1} same cryo-preserved Au-SLN samples exposed to NIR laser for 2 minutes as a measure of functional stability of the product; and (f) assessment of the hydrodynamic diameter of resuspended Au-SLN lyophilized cakes preserved for up to 6 months using 1% F-68 cryoprotectant. Error bars represent the mean ± standard error of the mean (SEM).

formed for 6 months, over which the morphology of the cake and TEM ultrastructure of Au-SLN were retained in both temperature conditions (Fig. 3c and S4) and took under a minute to obtain resuspended in Milli-Q. The UV-visible absorbance of Au-SLN samples where 1% F-68 was used as cryoprotectant showed a slight blue-shift in the absorbance maxima (Fig. 3d), while samples with 2.5% lactose as cryoprotectant displayed ideal intensity at absorbance maxima 750 nm (Fig. S5a). However, the photothermal profile of the samples with either cryoprotectant when irradiated with a laser at 750 nm and 650 mW for 2 minutes showed efficient heating from 50 to 60 °C for storage under both temperature conditions (Fig. 3e and S5b). The hydrodynamic diameter of samples was better preserved in samples stored at 4 °C than at 25 °C (Fig. 3f and Fig. S5c).

Au-SLN is well tolerated in the intracellular milieu and shows efficient photothermal death

It is crucial to conduct biocompatibility assessments before applying any formulation to *in vivo* studies. To this end, the

 This journal is © The Royal Society of Chemistry 2025

Published on 06 Agosti 2025. Downloaded on 03/10/2025 02:20:03.

Alamar assay was employed wherein non-fluorescent blue-coloured resazurin transforms into fluorescent pink-coloured resorufin. By measuring the intensity of resorufin, which indicates the metabolic activity of cells, cell viability can be determined. The biocompatibility study showed that Au-SLN was biocompatible up to 125 μg mL^{-1} in NIH3T3 and L929 non-cancer cell lines (Fig. 4a), with no observable morphological changes. Cytokinesis-block micronucleus assay was conducted to evaluate DNA damage and cytostatic properties of Au-SLN.[31] L929 mouse fibroblast cell line was used, and after the application of cytochalasin-B, a microfilament polymerization inhibitor, the cells were arrested at a binucleate phase to ensure the calculation of nuclear aberrations in cells that had undergone a single nuclear division cycle. With an increase in Au-SLN concentration, we observed an increase in the formation of nucleo-plasmic bridges and nuclear buds in binucleate cells; however, micronuclei formation was limited to 1% (Fig. 4 and S6), indicating no gross cytotoxic effect of Au-SLN up to 300 μg concentration.

To optimize the incubation time of Au-SLN *in vitro* for efficient intracellular uptake, we examined cell uptake using ICP-AES, photothermal efficacy post particle uptake *via* Alamar assay and cellular localization with TEM for breast cancer (BC) cell lines. Maximum nanoparticle uptake efficiency was observed for 9–12 hours post-incubation (Fig. 4c and Fig. S7a). TEM analysis of breast cancer cell lines revealed Au-SLN localization on the cell surface within multi-lamellar vesicles in the cytoplasm (Fig. 4d and e and Fig. S7b). EDX spectroscopy further confirmed the presence of gold within the cells (Fig. 4f and Fig. S7c). We confirmed photothermal efficiency after incubating 150 μg mL^{-1} of Au-SLN in 4T1, ZR-75-1 and MDA-MB-231 cell lines for 9–12 hours. NIR laser irradiation for 1 and 2 minutes resulted in a significant reduction in cell viability, achieving up to a 50% reduction after 2 minutes (Fig. 4g and Fig. S67e).

The thermal profile of Au-SLN recorded for different Au-SLN concentrations used for gross photothermal efficiency analysis is listed in Table S6. Gross photothermal efficiency had a direct correlation with an increase in nanoparticle concentration and NIR laser incidence time. Significant cell death (>75%, $p < 0.0001$) was observed across cell lines when PTT was conducted for 2 min at 150 μg mL^{-1} per well (Fig. 4h and Fig. S8). The mode of cell death after Au-SLN-mediated PTT was assessed using the classical Annexin V-PI experiment. The control groups exhibited around 95% cell viability, with less than 5% of the cells undergoing apoptosis. The group that received a sub-optimal dose of PTT exhibited around 65% of cells in the apoptotic phase and only 5% in the necrotic phase. In addition, the group that received the optimal dose exhibited around 17% cells in the necrotic phase, while ~54% of the cells were in the apoptotic phase (Fig. 4i). These results suggest that PTT induces cell death primarily through apoptosis at suboptimal temperatures, while optimal temperatures increase the percentage of the necrotic cell death (Fig. 4j). Moreover, PTT-induced DNA damage was assessed by immunofluorescence staining of γH2AX, which is an H2A protein variant that undergoes rapid phosphorylation at Ser139 by kinases, such as ATM and ATR, within minutes.[32] Distinct formation of γH2AX foci was observed in the nuclei of cells adjacent to the PTT-treated zone. In contrast, cells not exposed to PTT showed no γH2AX foci (Fig. 4k), implying that PTT effectively induced DNA damage in the targeted cancer cells.

Au-SLN shows excellent compliance for systemic toxicity as well as passive uptake in tumours

The hemocompatibility of nanoformulations is influenced by factors such as chemical formulation, zeta potential, and morphology.[33] Before pre-clinical efficacy testing, *ex vivo* hemocompatibility was assessed to determine a safe dose of administration in murine models. After incubating with various Au-SLN concentrations, the hemolysis percentage and RBC morphology were analysed. Samples with up to 300 μg of Au-SLN exhibited less than 5% hemolysis (Fig. 5a), which was found to be in compliance with the American Society for Testing and Materials (ASTM) E2524 guidelines. Environmental-SEM (E-SEM) analysis of glutaraldehyde-fixed RBCs showed no detectable adverse effects on RBC morphology (Fig. 5b), indicating that up to 300 μg of Au-SLN can be safely administered in pre-clinical murine models. Systemic toxicity and biodistribution assessments were performed in female Swiss bare mice by systemic administration *via* the intravenous route (Fig. 5c). No major adverse effects on the histopathology of vital organs were observed by hematoxylin & eosin (H&E) staining (Fig. S9). The major serum biochemical parameters reflecting the functioning of the vital organs also stabilized and became comparable to the controls by day 28 post injection (Fig. 5d).

The biodistribution of Au-SLN after systemic administration showed uptake in RES organs, including liver, kidney and spleen, at acute time points, with about 1.5% of the injected dose (ID) of gold detected per gram of liver tissue. None of the other vital organs harboured greater than a 1% injected dose per gram of respective tissue at any point in time post injection (Fig. 5e). Further, we assessed the passive targeting capability of Au-SLN. The % ID per gram of tissue when normalised over blood owing to systemic circulation indicated about 20% of the formulation accumulation at the tumour site (Fig. 5f). It may be noted that the biophysical characteristics of Au-SLN are such that they can passively accumulate at the tumour site systemically by virtue of the enhanced permeability and retention (EPR) effect.

IR Thermography and micro-CT imaging confirm that Au-SLN-mediated localised heating provides an excellent survival advantage when tumours are at an early stage

Au-SLN exhibited remarkable photothermal transduction and efficiency *in vitro*; however, these results do not adequately reflect the complexities of the tumour microenvironment and its influence on therapy outcomes. To address this challenge, a preclinical test was performed in a 4T1 orthotopic BC mouse model tagged with firefly luciferase-tdTomato fusion reporter (4T1-Fl2tdT) for non-invasive BLI-based progression assessment. In the PTT group, thermal elevation was tested using

Published on 06 Agosti 2025. Downloaded on 03/10/2025 02:20:03.

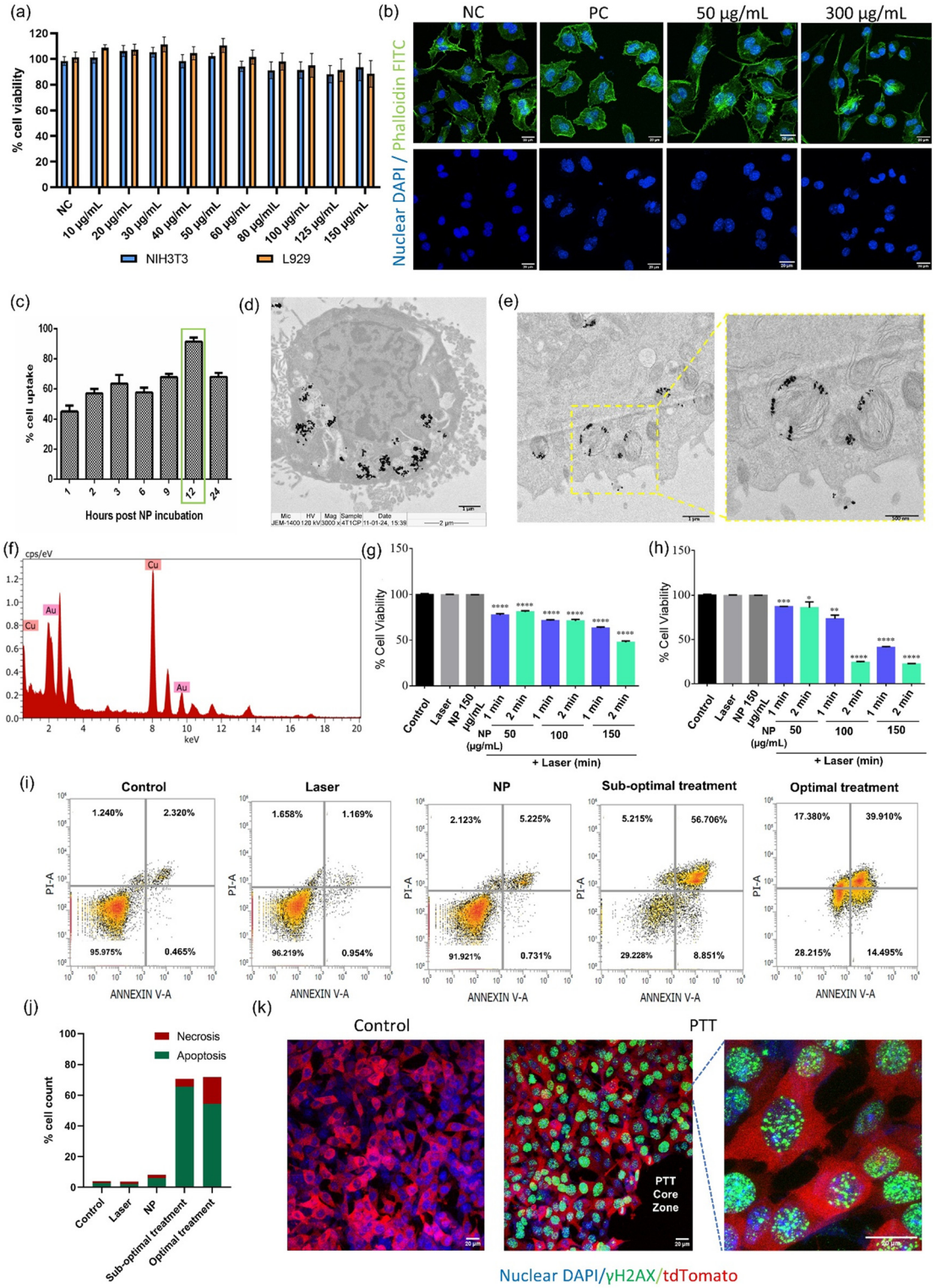

Fig. 4 (a) Biocompatibility evaluation of Au-SLN on NIH3t3 and L929 cell lines; (b) genotoxicity assessment on L929 cells by CBMN assay with cytochalasin-B treatment as the negative control (NC) and colchicine treatment as the positive control (PC). Scale bar denotes 20 µm; (c) ICP-AES measurement for Au-SLN uptake in 4T1 cells; (d) TEM imaging showing intracellular localization of Au-SLN in 4T1 cells. Scale bar denotes 1 µm; (e) TEM insets showing higher magnification of the intracellular localization of Au-SLN. Scale bar denotes 1 µm; (f) EDX spectra confirming gold uptake inside the 4T1 cell; (g) photothermal effect post Au-SLN uptake efficiency in 4T1 cells; (h) nanoparticle concentration and NIR laser time-dependent gross *in vitro* PTT efficiency in 4T1 cells; (i) mode of cell death as measured by Annexin V-PI staining in 4T1 cells; (j) tabulation of cell death mode; (k) γH2AX foci formation in the monolayer of 4T1 cells treated with PTT, indicating DNA damage post therapy acquired at 40× with zoomed-in inset showing γH2AX puncta formation in the nuclei. Scale bar denotes 20 µm. Error bars represent the mean ± standard error of the mean (SEM). *, **, ***, and **** indicate $p < 0.05$, 0.01, 0.001 and 0.0001, respectively.

 This journal is © The Royal Society of Chemistry 2025

Published on 06 Agosti 2025. Downloaded on 03/10/2025 02:20:03.

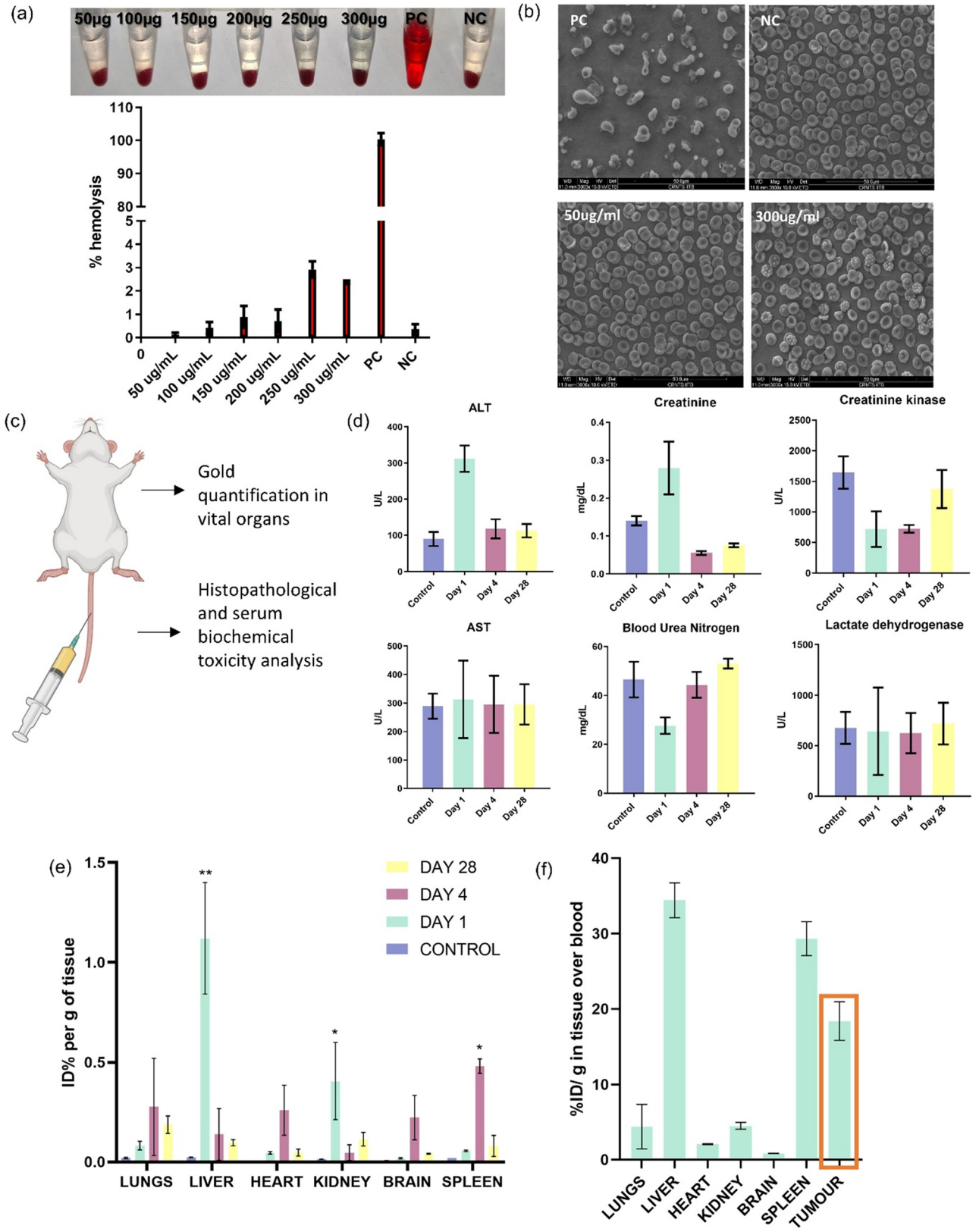

Fig. 5 (a) Hemolysis % analysis of Au-SLN; (b) E-SEM images of RBCs treated with the positive control (PC), negative control (NC), and 50 µg mL^{-1} and 300 µg mL^{-1} of Au-SLN. Scale bar denotes 50 µm. (c) Schematic for biodistribution and single dose systemic toxicity experiment set up in immunocompetent Swiss bare mice; (d) serum biochemistry analysis, and non-significant or $p \geq 0.05$ for vital organ functions; (e) ICP-AES-based quantification of gold in vital organs post systemic Au-SLN administration; (f) ICP-AES-based gold quantification for tumour homing of Au-SLN. Error bars represent the mean ± standard error of the mean (SEM) * and ** indicate $p < 0.05$ and 0.01, respectively.

Published on 06 Agosti 2025. Downloaded on 03/10/2025 02:20:03.

IRT images captured for 5 minutes with laser on/off conditions, showing the arrival of a peak temperature of 67.5 °C at the Au-SLN-injected tumour site within 4 minutes, which rapidly returned to physiological levels within one minute after the laser was turned off (Fig. 6a and b). In comparison, the mice in the control cohort did not exhibit any significant temperature increase (Fig. S10). This localized heating is essential to selectively ablate tumour cells while minimizing damage to the surrounding healthy tissue, thereby enhancing both the safety and efficacy of the treatment. Moreover, the control group was monitored up to day 7 (corresponding to 15–18 days post-tumour induction), at which point the mice were euthanized owing to tumour necrosis, in accordance with ethical guidelines.

Further investigation by tomographic molecular imaging application was pivotal for evaluating the volumetric effects of PTT, capitalizing on its abilities for depth perception and anatomical localization of the tumour mass. The efficacy of PTT in tumour debulking was assessed in female CD1-nude mice bearing 4T1-Fl2tdT tumours using micro-computed tomography (micro-CT), alongside planar BLI (2D-BLI) measuring live tumour cell mass at different time points. Micro-CT provided detailed volumetric assessments on early-stage tumours (volume less than 50 mm^3), wherein tumour volume dipped to less than 10 mm^3 ($p = 0.0004$) following a single dose of PTT. However, within a week post treatment, the volume at the primary tumour site increased owing to localized swelling and burn scab formation typical of thermal responses[34,35] correlating with visual evaluations. Meanwhile, BLI-quantified luminescence decreased from e^9 to e^3 orders of magnitude (average radiance from 1.34×10^9 to 1.2×10^3 photons per second per cm^2 per steradian, with $p = 0.0029$) post treatment, which confirmed substantial tumour debulking (Fig. 6c–e), leading to subsequent reduced swelling and healing at the tumour site. Notably, mice treated with PTT exhibited stark survival improvement, from 15 days of survival in the control group to >50 days in the treatment group, owing to rapid tumour regression over time (Fig. 6f) as complete remission was achieved, underscoring the potential of Au-SLN-mediated PTT as an effective intervention for early-stage tumours.

The advantage of using multimodal imaging techniques depends on their ability to provide comprehensive insights into both tumour viability and metabolic functional changes, allowing for a more thorough evaluation of treatment efficacy. Therefore, we further employed imaging procedures, such as planar fluorescence imaging (2D-FLI), utilizing NIR fluorophore for 2-deoxyglucose (2-DG), Fluorescence Light Imaging Tomography (FLIT or 3D-FLI) and Diffuse Light Imaging Tomography (DLIT or 3D-BLI) to analyse the effects of photothermal therapy on tumour progression (Fig. 7a and Fig. S11). After treatment, significant reductions exceeding two-log folds in tumour volume were observed by both 2D-BLI and DLIT ($p = 0.0014$ and $p = 0.0015$, respectively) (Fig. 7b and c). Imaging assessments indicated an initial decrease in tumour post-PTT; however, these results highlighted the need for careful interpretation, as the reduction in volume alone does not guarantee long-term therapeutic success. In addition to volume reduction, we also observed a notable decrease in glucose metabolism quantified by 2D-FLI and FLIT ($p = 0.0017$ and $p = 0.0433$, respectively), which decreased up to two-fold post treatment within the tumours, indicating an immediate impact on tumour viability (Fig. 7d and e). This reduction suggests that PTT effectively disrupts the metabolic processes of cancer cells. Despite these positive outcomes, challenges emerged when treating larger tumours (>75 mm^3) with a single dose of PTT. The initial response indicated effectiveness; however, many tumours exhibited tumour growth recurrence within a short span of three to five days post-PTT, leading to decreased survival rates compared to small-sized tumours (Fig. 7f). Tumour relapse underscores the limitations of relying solely on single-dose therapies for larger or more aggressive tumours and highlights the necessity for additional treatment strategies to enhance long-term outcomes.

For large-sized tumours, repeat doses of PTT improve the survival outcome of mice

Administering multiple booster doses of PTT is essential for enhancing treatment efficacy, particularly in larger or more aggressive tumours. These repeated doses help overcome the challenges associated with tumour resilience and ensure more effective tumour ablation (Fig. 8a). Larger tumour volumes (≥75 mm^3) present significant challenges compared to ablation of smaller tumours (Fig. 8b). Although a single dose may improve the longevity of treated mice, they often need to be sacrificed owing to the failure of complete tumour mass eradication. Large and aggressive tumour types, such as 4T1 mouse breast cancer, frequently exhibit a quick rebound within days post-treatment. This necessitates a more aggressive treatment approach to manage tumour growth effectively. Therefore, we utilized female NOD-SCID mice implanted with 4T1-Fl2tdT tumours and attempted non-invasive BLI-guided monitoring of tumour growth while trying repeated PTT procedures (Fig. 8a). After the first PTT dose on day 0, a significant reduction of up to 10-fold ($p = 0.0037$) in average radiance at the primary tumour site was noted. To ensure complete tumour eradication, repeated PTT doses were administered to the remaining tumour mass on day 3 and day 5. Following booster doses, BLI showed significant tumour regression over a week, with average radiance decreasing over 6 log-folds ($p = 0.0126$) and without the sign of recurrence (Fig. 8c). Healing of the tumour site occurred within 15 days, with no adverse side effects observed. This substantial reduction underscores the effectiveness of the treatment regimen. Moreover, mice in the treatment group exhibited improved survival outcomes compared to those in the control groups, which were sacrificed owing to tumour burden at a much earlier time point (Fig. 8d). The experiment demonstrated that Au-SLN-mediated PTT monotherapy can effectively ablate solid tumour masses, thereby improving overall survival outcomes in a preclinical setting.

 This journal is © The Royal Society of Chemistry 2025

Published on 06 Agosti 2025. Downloaded on 03/10/2025 02:20:03.

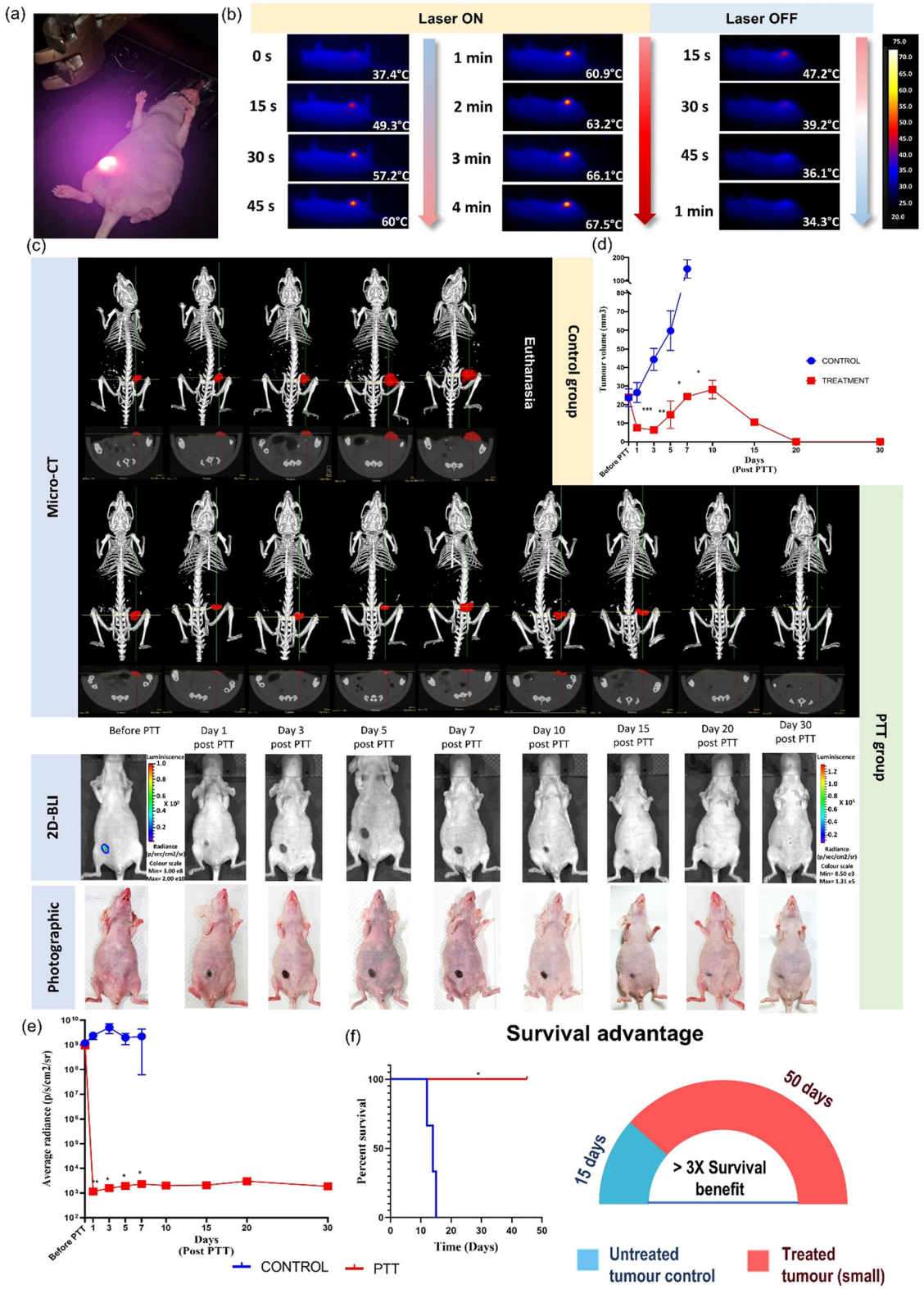

Fig. 6 Non-invasive measurement of *in vivo* thermal conversion and therapeutic effects of Au-SLN in early-stage tumours. (a) Photograph showing a mouse undergoing PTT; (b) representative IRT photograph showing change in temperature measured with laser turn on/turn off conditions as marked; (c) micro-CT, 2D-BLI and photographic image of representative mice bearing small sized tumour undergoing therapy trial assessment using single dose of PTT; (d) measured tumour volume recorded for control and treatment group using micro-CT; (e) average BLI signal quantified from the control and treatment groups of mice over the entire period of experiment; and (f) survival analysis of PTT-treated mice with a small tumour, with side panel highlighting mice longevity increased over three folds in the PTT-treated group. Error bars represent the mean ± standard error of the mean (SEM). *, **, and *** indicate $p < 0.05$, 0.01 and 0.001, respectively.

Published on 06 Agosti 2025. Downloaded on 03/10/2025 02:20:03.

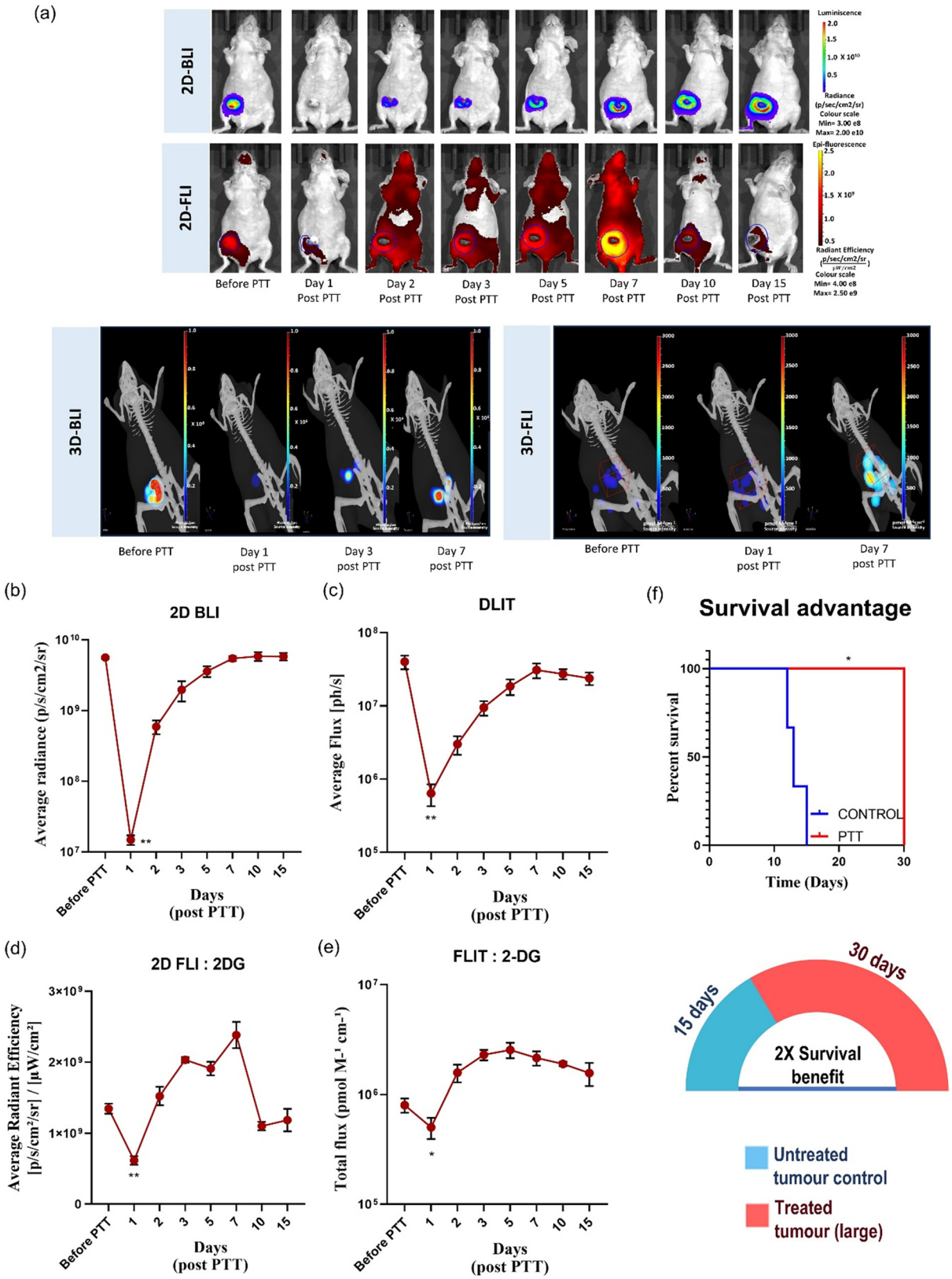

Fig. 7 (a) 2D-BLI, 2D-FLI, 3D-BLI (DLIT), and 3D-FLI (FLIT) assessment of tumour depletion and glucose metabolism in mice bearing large tumour; (b) 2D-BLI; (c) DLIT; (d) 2D-FLI; (e) FLIT quantitation measured from tumour site; (f) survival analysis post-PTT dose in mice bearing large tumour, with bottom panel highlighting mice longevity doubled in PTT-treated cases with large tumours. Error bars represent the mean ± standard error of the mean (SEM). * and ** indicate $p < 0.05$ and 0.01, respectively.

 This journal is © The Royal Society of Chemistry 2025

Published on 06 Agosti 2025. Downloaded on 03/10/2025 02:20:03.

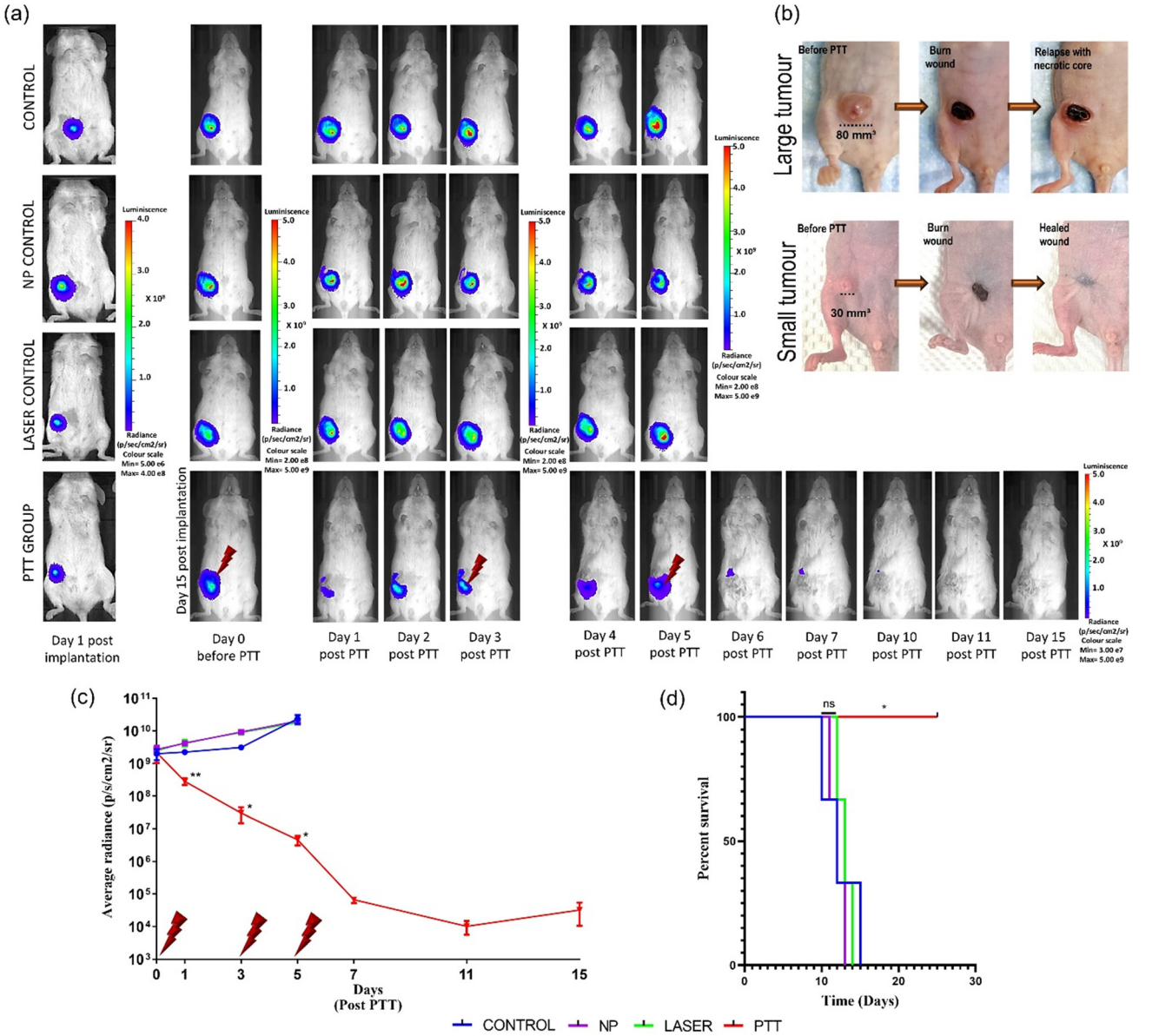

Fig. 8 (a) Representative BLI images of mice with advanced orthotopic tumours on different days in the control, NP control, laser control and PTT groups as indicated; (b) photographic representation of mice bearing small and large tumours at different stages of impact monitoring after single PTT treatment; (c) graph showing the average BLI signal quantitated from all mice in each group; (d) Kaplan Meier survival graph for each group. Error bars represent the mean ± standard error of the mean (SEM). * and ** indicate $p < 0.05$ and 0.01, respectively.

Post-treatment fate of Au-SLN and aftermath in residual tumour

To ensure that Au-SLN is effectively cleared from the body, we investigated the body elimination properties of the material. Urine samples were collected at specific intervals, while kidney and tumour tissues were analysed at terminal time points. ICP-MS analysis revealed significant gold content in urine from the PTT group compared to the material control group (Fig. 9a). TEM and EDS identified approximately 5 nm gold nanoparticles in urine and kidney samples (Fig. 9b–d), indicating accelerated degradation when the material is exposed to laser and thus renally cleared post-treatment. Additionally, TEM and EDS of tumour tissue showed both intact and disintegrated Au-SLN after near-infrared (NIR) laser exposure, underscoring its disintegrable properties (Fig. 9e and f and Fig. S12).

The Au-SLN's significant photothermal effects prompted an investigation into structural changes in tumours post-PTT. Tumour specimens analysed using TEM revealed a severe loss of cellular integrity and destruction of the extracellular matrix at the treatment site (Fig. 9e and f). H&E staining further demonstrated a loss of tissue integrity, particularly in the laser-incident area compared to distant regions. Epidermal dissociation and collagen deposition were also observed, indicating charring and

Published on 06 Agosti 2025. Downloaded on 03/10/2025 02:20:03.

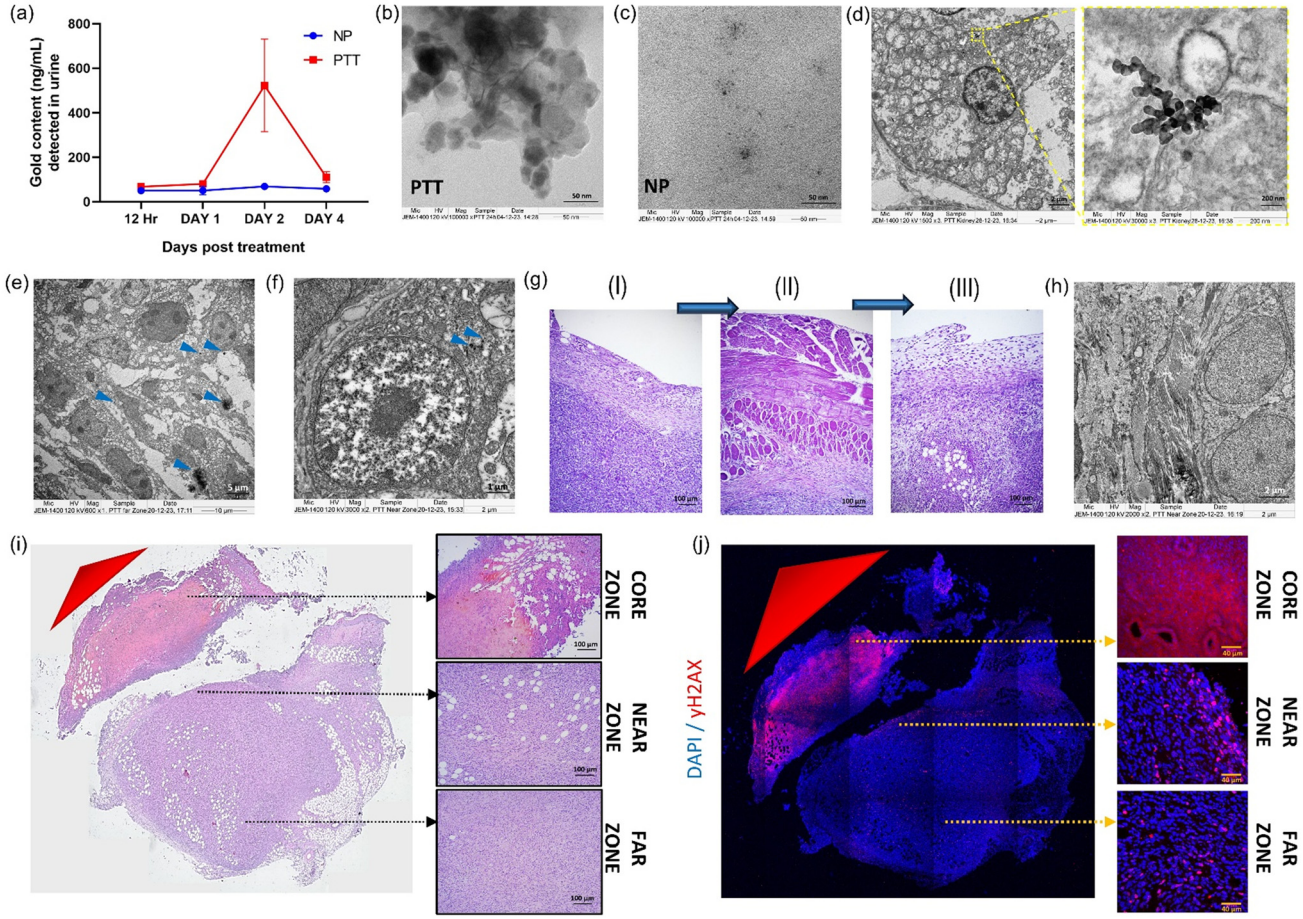

Fig. 9 (a) Quantitation of gold detected in urine by ICP-MS to evaluate renal clearance post treatment; (b) TEM of gold in the urine sample of PTT group observed one hour post PTT. Scale bar denotes 50 nm. (c) TEM of gold in the urine sample of the nanoparticle control group observed 48 hours post administration. Scale bar denotes 50 nm; (d) TEM of the kidney section showing Au-SLN post treatment confirming renal clearance. Scale bar denotes 2 μm, and the scale bar of the inset is 200 nm. (e) and (f) TEM of cellular and tissue integrity loss in the tumour section treated with PTT. Blue arrows indicate the disintegrated gold nanoparticles detected. Scale bar denotes 5 μm and 1 μm for (e) and (f), respectively. (g) H&E of transition from solid subcutaneous breast tumour before treatment (I) to post-treatment epidermal dissociation and collagen deposition indicating healing post-PTT (II) and, finally, healed skin formation at the mammary fat pad (III); scale bar denotes 100 μm. (h) TEM ultrastructure of collagen deposition at the treated site; scale bar denotes 2 μm. (i) IHC of the tumour section showing zones of ablation from the site of laser incidence shown in brown, and the zoomed-in image is a stitched tile scan of the whole tumour, insets of core, near and far zone acquired at 10×. Scale bar denotes 100 μm. (j) Immunofluorescence staining for γH2AX to observe the extent of DNA damage as per zones of ablation, zoomed-in image is a stitched tile scan of the whole tumour, and insets of the core, near and far zone acquired at 60×. Scale bar denotes 40 μm. Error bars represent the mean ± standard error of the mean (SEM).

healing (Fig. 9g and h). These findings suggest that burn wounds induced by PTT heal rapidly, as confirmed by long-term efficacy assessments that show successful recovery in mice.

Furthermore, PTT-induced DNA damage was evidenced by positive staining for γH2AX foci (Fig. 9i and j) in the core treatment zone. Necrotic patches in the core tissue resulted in smeared γH2AX staining, while adjacent untreated zones displayed prominent foci owing to less thermal insult.

Conclusions

In this work, a novel gold-coated solid lipid nanoparticle (Au-SLN) was developed, demonstrating high photothermal conversion efficiency under low-powered (650 mW) laser excitation settings. The simple solvent emulsion evaporation method-based Au-SLN synthesis protocol showed high reproducibility and upscale production ability with long-term storage. Moreover, the formulation demonstrated extended stability for up to six months post-lyophilization, thereby enhancing its biomedical application potential. Comprehensive safety evaluations, including biocompatibility, hemocompatibility, and genotoxicity assessments for Au-SLN, confirmed preclinical safety measured with no adverse effects in vital organs, even at concentrations above therapeutic requirements. The nanoparticle showed efficient cellular uptake within 9–12 hours in the breast cancer cell lines tested, indicating favourable therapeutic timing windows for *in vivo* applications.

 This journal is © The Royal Society of Chemistry 2025

Published on 06 Agosti 2025. Downloaded on 03/10/2025 02:20:03.

Our *in vivo* preclinical investigations revealed the potential and current limitations of Au-SLN-mediated photothermal therapy. Although IR thermography demonstrated precise control over fast thermal elevation to >60 °C at the site of laser incidence for less than 4 minutes, the temperature drops back to normal within a minute by turning off the laser. The integration of multimodal imaging, including micro-CT, bioluminescence, NIRF and tomographic molecular imaging estimations, provided comprehensive insights into PTT treatment outcome. IRT enabled real-time monitoring of localized hyperthermia; microCT provided detailed anatomical and volumetric analysis; BLI/DLIT allowed sensitive, 3D tracking of viable tumour progression; NIRF/FLIT offered high-resolution visualization of fluorescent markers, precisely assessing tumour metabolic activity *via* 2DG uptake. This integrated approach enabled cross-validation, precise monitoring of both anatomical and functional changes, and the robust evaluation of Au-SLN-mediated PTT efficacy. The results revealed that a single dose of PTT can cause a significant reduction in tumour volume and/or metabolic decline, offering a more nuanced understanding of therapeutic efficacy. However, the treatment efficacy showed notable tumour size-dependent variation. Early-stage tumours (<50 mm^3) exhibited a superior response, showing complete healing with no sign of recurrence over a significant period, while tumour masses larger than 80 mm^3 showed a requirement of multiple booster treatments to control the tumour growth, a challenge that can also be relevant for the treatment of advanced-stage tumours in clinical cases. In either situation, the life expectancy of mice showed significant improvement and implementation of multiple treatment doses addressed the limitations observed for single-dose standalone PTT treatment. Additionally, it is worth noting that none of the mice that underwent PTT showed any noticeable sign of distress owing to secondary infection at the site of treatment, which always healed within a few days.

The demonstrated success in treating smaller and larger tumours using Au-SLN-mediated photothermal therapy suggests a potential standalone application for early-stage treatment or as an adjuvant therapy to debulk large primary tumours, where, in either case, pronounced survival benefits can be achieved. Additionally, the established safety profile and efficient cellular uptake support the exploration of combination therapies,[36,37] potentially enhancing outcomes in cases of larger or more aggressive tumours. Looking ahead, this generated platform has the potential to serve as a springboard for next-generation cancer therapeutics. Enhanced particle design using suitable targeting moieties and advances in laser technology can also be performed to improve the tissue penetration depth. A combinatorial approach[38] with other conventional or emerging therapeutics may potentially help to overcome the current limitation of tackling large-sized tumour masses. The integration of artificial intelligence for treatment planning and real-time monitoring will enable personalized dosing strategies, while advances in laser technology will improve tissue penetration depth.

Materials and methods

Chemicals and reagents

Glyceryl palmitostearate (UNII Code (FDA): 73071MW2KM) from Gattefossé; L-ascorbic acid (#100468), hydrochloric acid (#100317), nitric acid (#100456), D-mannitol (#105983), lactose (#107657), trehalose (#108216), sucrose (#107657), tween-80 (#822187), colchicine (#PHR1764), formaldehyde solution 37% (#1.94900.0521) from Merck, India; tetrachloroauric acid (HAuCl4) (#010745-1G) from Spectrochem, India; stearyl amine (#305391), resazurin sodium salt (#R7017-5G), cytochalasin-B (#C6162-1MG), DAPI (#D-8417-10MG), paraformaldehyde (#P6148), glutaraldehyde (#49629) from Sigma-Aldrich, India; Triton X-100 (#194854) from MP Biomedicals, India. Poloxomer-188 (#30631540), Cremophore EL (#30554032) and pluronic F-68 (#30631540) were generous gifts from BASF chemicals, India. Roswell Park Memorial Institute media (RPMI-1640, #31800-022), Dulbecco's modified Eagle's medium (DMEM, #12800-017), fetal bovine serum (FBS, #RM10409), penicillin–streptomycin (#1A002A-5X100 mL) from Gibco, USA; HiSepTM LSM 1077 (#LS001), Tris-EDTA (#MB011), BSA (#MB083) and dialysis membrane from HiMedia, India; Annexin V-PI kit (#ab214485) from Abcam, USA; XenoLight Rediject 2-DG-750 (#760561) from Revvity, India; D-Luciferin (#L-8220) from Biosynth, India; FITC-phalloidin (#50U 00042-T) from Alliance Bio, India; anti-rabbit DyLight™ 633 secondary antibody (#35562), anti-rabbit DyLightTM 488 secondary antibody (#35552), ImmunoPure normal goat serum (#31872) from Thermo Fisher Scientific, India; osmium tetroxide (OsO4) from Electron Microscopy Sciences, Hatfield, USA; araldite resin from Ted Pella, Inc., USA; anti-phospho-histone γH2A.X rabbit monoclonal Ab (Ser139) (20E3) (#9718) from Cell Signaling Technology; sodium borohydride (#1948108) from SRL, India; Vectashield Antifade Mounting Medium (#H-1000) from Vector Laboratories, India.

Cell culture

4T1 mouse and ZR-75-1 human breast cancer cells were cultured in RPMI-1640 media. L929, NIH3T3 and MDA-MB-231 cells were cultured in DMEM supplemented with 10% FBS and 1% penicillin and streptomycin and incubated at 37 °C and 5% CO_2 conditions for all lines. The Fluc2-TdTomato fusion reporter labelled 4T1 cell line (4T1-Fl2tdT) was generated previously in our lab.[39] Reporter labelled human breast cancer cell line MDA-MB-231-Luc2 cells (#119369) were procured from PerkinElmer, India.

Au-SLN synthesis

A solid lipid nanoparticle was synthesized using the solvent emulsion evaporation method. The aqueous phase was prepared by dissolving 2% surfactants (1% cremophore EL and 1% Tween-80) and 10% sucrose in deionized water. The organic phase was prepared by dissolving glyceryl palmitostearate and stearyl amine in a 5 : 1 ratio in the organic solvent chloroform. For the emulsion reaction mixture, one-fifth of

Published on 06 Agosti 2025. Downloaded on 03/10/2025 02:20:03.

the organic phase was added gradually to the aqueous phase, maintaining a flow rate of 0.1 mL per minute using a syringe pump under homogenization at 13000 rpm. The crude emulsion thus formed was then sonicated at 50% amplitude with 5 second ON/2 second OFF cycles for 10 minutes at 2–8 °C, yielding a milky white solution. The emulsion was immediately subjected to organic solvent evaporation using a rotary evaporator with a bath temperature of 45 °C and 150 rpm. The pressure gradually decreased at 50 millibar per minute to achieve complete chloroform evaporation, as confirmed by the transformation of the emulsion colour from milky white to transparent. The prepared SLN was then dialyzed with Milli-Q at 2–8 °C for 8 hours with intermittent renewal of the external media to remove any unreacted precursor molecules. For the gold coating of SLN, a freshly prepared 20 mM ascorbic acid and 2.5 mM gold chloride (HAuCl4) solution were prepared. To tune these gold-based nanoparticles to the near *infra*-red (NIR) wavelength, the core (SLN) to shell (gold coating) principle was employed.[19,40] For a small reaction mixture, in the presence of 1 mL ascorbic acid, 150 μL of the gold solution was added to 75 μL of SLN while vortexing at 100 ± 200 rpm at room temperature under a halogen lamp. The shift in the colour of the solution from colourless to deep navy blue indicated the formation of gold-coated solid lipid nanoparticles tuned for peak absorption at 750 nm, which was confirmed by UV-Visible spectrophotometry. The reaction mixture was then scaled up by a 1 : 1 increase in the volumetric ratio of ascorbic acid, gold chloride solution and SLN. The Au-SLN was then dialyzed with Milli-Q at room temperature for at least 10–12 hours to remove unreacted gold chloride and enhance the purity of the Au-SLN solution. To enhance the stability of Au-SLN in the colloidal state, a 1% Poloxomer-188 surfactant was added to the solution and stored at 4 °C for up to a month for experiments. Various batches of Au-SLN were synthesized and characterized to verify reproducibility and scale-up.

Au-SLN size, zeta-potential and λ^{Max} analysis

The size distribution and zeta potential of Au-SLN were evaluated using NanoStar DLS v2.3.6.3 (Wyatt Technologies, USA) and Zetasizer Nano ZS (Malvern Instruments, United Kingdom), respectively. The UV-Vis spectrum of the nanoparticles was recorded using a PerkinElmer spectrophotometer (Lambda 25, USA).

Electron microscopy analysis

The morphological evaluation of the nanoparticles was carried out with a field emission gun scanning electron microscope (FEG-SEM, JSM-7600F, Jeol Ltd, Japan), field emission gun transmission electron microscope (FEG-TEM, JEM-1400), and TEM (JEOL 1400 plus TEM, Japan). The morphology of red blood cells (RBCs) was characterized using environmental-scanning electron microscopy (ESEM, Quanta 200, FEI, Austria). Nanoparticle localization in 4T1 and ZR-75-1 cells, tumour and kidney ultrastructure post PTT was analysed using bio-TEM. *Ex vivo* tissue samples and cells incubated with Au-SLN were washed and pre-fixed using 3% glutaraldehyde solution in cacodylate buffer (pH 7.2) for two hours. Following this, the cells were fixed in a 1% OsO_4 solution for 2 hours in a cold environment. The cells were then dehydrated using a series of graded ethanol solutions and subsequently embedded in Araldite resin, followed by heat polymerization for 72 hours. Ultra-thin sections of 70 nm were prepared utilizing an ultramicrotome (Leica UC7, Germany) and placed on copper grids. Microphotographs were captured using JEOL 1400 plus TEM, Japan, at 120 kV.

Determination of photothermal conversion efficiency and multicyclic PTT efficiency

For photothermal conversion efficiency measurements, 3 mL of 50 mg mL^{-1} Au-SLN was placed in a standard quartz cuvette. The sample was irradiated with a 750 nm NIR laser at 650 mW, and temperature changes were monitored until a steady state was achieved. The photothermal conversion efficiency (η) of Au-SLN was then calculated using the following formula:[17,41]

$$\eta = \frac{hS(T_{Max} - T_{Surr}) - Q_{Dis}}{I(1 - 10^{-A750})},$$

where h is the heat transfer coefficient, S is the sample well surface area, T_{Max} is the steady-state maximum temperature attained by Au-SLN, T_{Surr} is the room temperature, Q_{Dis} is the baseline energy input, I denotes the laser power, and $A750$ is the absorbance of Au-SLN at 750 nm.

For multicyclic PTT stability experiments, 100 μL of 50 mg mL^{-1} Au-SLN was aliquoted into individual wells of a 96-clear well plate. The same NIR laser parameters (750 nm and 650 mW) were used, and temperature changes were recorded over three consecutive repeated irradiation cycles. This process was repeated for up to three consecutive cycles to verify the material's photothermal stability of the material. Particle morphology post-multiple cycles was observed using TEM.

Photothermal transduction of Au-SLN

To analyse the impact of nanomaterial concentration, laser power and laser incidence duration on the photothermal transduction potential of Au-SLN, face-cantered central composite design (CCD) was employed. A CCD of 17 runs of different values for the independent variables was selected. For each run, 100 μL of Au-SLN was placed in a 96-well plate, and the response temperature was recorded. Using Design of Expert (Design-Expert, 11.0.3.0), the effect of the independent factors on the response element was estimated.[17]

Optimization of Au-SLN lyophilization and long-term storage conditions

Lyophilization was optimized using F-68 and cryoprotectants (lactose, mannitol, sucrose, and trehalose) at 1, 2.5, and 5%. The Au-SLN solutions were snap-frozen in liquid nitrogen, lyophilized for 48 hours, and then reconstituted in Milli-Q water for stability analysis using UV-visible spectroscopy (λ^{Max} 750 nm) and DLS for hydrodynamic diameter and polydispersity index. Lyophilized samples stored at 4 °C and 25 °C with

 This journal is © The Royal Society of Chemistry 2025

Published on 06 Agosti 2025. Downloaded on 03/10/2025 02:20:03.

55–60% relative humidity were tested at 1, 2, 3, and 6 months for stability using DLS and UV-Visible absorbance as well as thermal profile.

Biocompatibility evaluation of Au-SLN

Approximately 5000 cells (NIH3T3 and L929 cell lines) were seeded in 96-well plates and incubated overnight. Cells were exposed to a long range of Au-SLN concentration between 10 and 150 μg mL^{-1}, with culture medium as a control. After 24 hours, cell viability was evaluated using the Alamar assay. Resazurin sodium salt (10 μL of 1 mg mL^{-1}) was added, and fluorescence intensity was measured at 560 nm (excitation λ^{Max}) and 590 nm (emission λ^{Max}) to evaluate the cell viability using the following equation:

$$\text{Cell viability}\,\% = \frac{\text{fluorescence intensity of test sample} - \text{fluorescence intensity of blank}}{\text{fluorescence intensity of negative control} - \text{fluorescence intensity of blank}} \times 100.$$

Cell viability assessments

To analyse efficient intracellular uptake of Au-SLN, 4T1, ZR-75-1, and MDA-MB-231 cell lines were incubated with 50 μg mL^{-1}, 100 μg mL^{-1}, and 150 μg mL^{-1} of Au-SLN for 9–12 hours and then washed off. 750 nm with a 650 mW NIR laser was irradiated for 1 and 2 minutes. Cell viability assessment was performed using the Alamar assay.

Gross photothermal efficiency was tested in the same cell lines by seeding in a 96-well plate at 5000 cells per well. 50 μg mL^{-1}, 100 μg mL^{-1}, and 150 μg mL^{-1} of Au-SLN were added with no incubation time/washing, ensuring the presence of the entire Au-SLN concentration in the wells, and irradiated with a 650 mW 750 nm NIR laser for 1 and 2 minutes. Post-PTT, therapy efficacy was assessed using the Alamar assay.

Cell death analysis

Cellular apoptosis in the PTT-treated 4T1 and ZR-75-1 cell populations was determined by staining with FITC-conjugated Annexin V-PI. Approximately 3 × 105 cells per mL were plated in 35 mm dishes for different groups: untreated control, laser, nanoparticle (NP) controls and treatment group. 50 μg mL^{-1} Au-SLN was added to the cells in the nanoparticle and treatment groups. Laser (750 nm and 650 mW) was irradiated to achieve sub-optimal (50 ± 1 °C) and optimal (55 ± 1 °C) temperatures. After 24 hours, the cells were stained with Annexin V and PI and analysed by applying an Attune NxT Flow cytometer (Invitrogen).

Hemocompatibility assessment of Au-SLN

A human blood sample was obtained from a healthy volunteer in EDTA-coated tubes in accordance with ethical guidelines after approval from the Institutional Ethics Committee (IEC) at IIT-Bombay (IITB-IEC/2021/024). Informed consent was obtained from the human participants before sample collection. Intact RBCs were isolated from whole blood by 1 : 1 dilution with PBS (pH 7.4), followed by centrifugation at 1000 rpm and 4 °C for 5 min for multiple rounds. Different concentrations of Au-SLN prepared were incubated with 200 μL of RBCs at 37 °C for 3 hours. PBS was used as a negative control, and Triton X-100 was used as a positive control. Post incubation, the samples were centrifuged at 1000 rpm and λ^{Max} of the supernatant was recorded at 540 nm to calculate the hemolysis % using the following formula:

$$\text{Hemolysis}\,\% = \frac{\text{absorbance of test sample} - \text{absorbance of negative control}}{\text{absorbance of positive control} - \text{absorbance of negative control}} \times 100.$$

The RBCs were fixed overnight using 2% glutaraldehyde at 2–8 °C and subjected to morphological analysis using E-SEM.

Genotoxicity assessment of Au-SLN

This was evaluated in L929 mouse fibroblast cells using the cytokinesis-block micronucleus assay.[31] 1.5 × 10^5 cells were seeded over a coverslip in a 6-well plate and serum-starved overnight. The cells were then given simultaneous treatment of 1 μg mL^{-1} cytochalasin-B and Au-SLN of different concentrations ranging from 50 to 300 μg mL^{-1} and incubated for 24 hours. Colchicine (1 μM) along with cytochalasin-B was used as a positive control, while cells treated only with cytochalasin-B were used as a negative control. Post-treatment, the cells were fixed in 4% paraformaldehyde. 2% BSA was used for blocking, followed by FITC-phalloidin and DAPI staining of the cells. The coverslips were mounted on slides using Vectashield and stored at −20 °C in a humid chamber until analysis using a Nikon AX confocal microscope.

Systemic animal toxicity and homing of Au-SLN

All animal experiments were in accordance with the protocol (29/2021) that received approval from the Institutional Animal Ethics Committee (IAEC) at ACTREC. Systemic animal toxicity was tested on healthy female Swiss bare mice (~20 g) from ACTREC-TMC, Mumbai, following CPCSEA guidelines. Mice were divided into control and test groups for days 1, 4, and 28 (n = 3 per group). Test mice received 300 μg nanoparticles *via* tail vein injection (intravenous), while controls received PBS. Blood and major organs were collected post-sacrifice, and samples were submitted to the Composite Lab, ACTREC, for serum biochemical analysis, histological examination in the Laboratory Animal Facility ACTREC, and ICP-AES analysis for gold quantification. Serum was evaluated for a range of biochemical parameters, including liver function indicators, such as serum glutamic oxaloacetic transaminase/aspartate amino transferase (SGOT/AST) and serum glutamic pyruvic transaminase/alanine amino transferase (SGPT/ALT). To assess nephrotoxicity, the levels of blood urea nitrogen (BUN) and creatinine were measured. Additionally, myocardial lesions, anaemia, and other conditions were assessed by measuring the levels of creatinine phosphokinase (CKI) and lactate dehydrogenase (LDH). For histopathology, paraffin-embedded formalin-fixed organs and tumours were sectioned into 5 μm thick micro-

Published on 06 Agosti 2025. Downloaded on 03/10/2025 02:20:03.

tome sections. They were stained with H&E and imaged using a Zeiss Axis Imager Z1 microscope.

Gold quantification

Gold quantification of Au-SLN batches, cell uptake studies, animal biodistribution and tumour homing studies was carried out with inductively coupled plasma atomic emission spectroscopy (ICP-AES, SPECTRO Analytical Instruments GmbH, Germany). To quantify intracellular uptake, breast cancer cell lines 4T1, ZR-75-1, and MDA-MB-231 were incubated with 50 μg mL^{-1} of the nanoformulation for 1 to 24 hours. The cells were digested in aqua regia for quantitation. For animal biodistribution, vital organs and blood samples were collected during the toxicity experiment and digested in aqua regia for quantitation. To assess the tumour homing of Au-SLN, female CD1 nude mice (n = 3) bearing 4T1orthotopic tumour received 180 μg of Au-SLN *via* systemic i.v. administration. Mice were euthanized after 24 hours, and their blood, tumour, and vital organs were collected for gold quantitation by ICP-AES. For the material clearance of the urine samples, inductively coupled plasma mass spectrometry (ICP-MS, Thermo Fisher Scientific, Germany) was used for improved gold detection sensitivity.

In vitro and *in vivo* assessments of DNA damage

ZR-75-1 and 4T1-Fl2tdT cells were seeded at a density of 0.5 million cells per mL over a coverslip in a 35 mm dish. 10 μg mL^{-1} Au-SLN was added, and a 750 nm and 650 mW laser was incident for 2 min. After 24 hours, cells were fixed with 4% formaldehyde, permeabilized with Triton-X 100 and blocked with 5% BSA. The cells were incubated with anti-phospho-histone γH2A.X antibody at a dilution of 1 : 200 at 4 °C overnight in a covered, humid chamber. The next day, the cells were washed and incubated with a DyLightTM 488 secondary antibody. Nuclear counterstaining was performed with 1 μg mL^{-1} DAPI (1 : 200 dilution) for 1 min under dark conditions. The coverslips were mounted using Vectashield and proceeded for fluorescence imaging using a Leica SP8 confocal microscope. Image analysis was performed using ImageJ software. For *in vivo* γH2AX staining, orthotopic 4T1 tumours were excised after PTT, fixed in 10% formalin and processed for sectioning. Tissue sections were dehydrated, followed by antigen retrieval. Slides were incubated overnight with γH2AX primary antibody (1 : 200 dilution) at 4 °C, followed by incubation in anti-rabbit DyLight™ 633 secondary antibody. After DAPI nuclear counterstaining, sections were mounted with Vectashield and imaged using a confocal LSM780 microscope.[32]

In vivo infrared thermography

4T1-Fl2tdT orthotopic tumour bearing mice were divided into control, nanoparticle control, laser control, and treatment groups (n = 3 each). Fourteen days post implantation, 180 μg/100 μL Au-SLN was injected intratumourally, and 30 minutes later, the mice were anesthetized using 2% isoflurane gas anaesthesia. PTT was performed using a 750 nm laser at 650 mW for 4 minutes as optimized. Dynamics of temperature elevation was video-graphed using IR camera ThermCam 160 (Specialize Products Pvt. Ltd, India). After 4 minutes, the laser was switched off, but IR thermographic capture continued for another minute. The captured data were analysed using the Infraview software provided by the camera.

Micro-CT *in vivo* imaging

Therapy efficiency *in vivo* was measured in female CD1 nude mice bearing early-stage 4T1-FL2tDT orthotopic tumours (≤50 mm^3). Mice were divided into control and treatment (n = 4) groups for microCT analysis. For PTT, mice were injected intratumourally with 180 μg/100 μL of Au-SLN, followed by a 4 minute NIR laser treatment (750 nm and 650 mW). To measure anatomical change in tumour mass before and after a single PTT dose, micro-CT imaging (Quantum GX2 microCT, Revvity) was performed in anaesthetized mice. Analyse 14.0 software was used for the image data analysis.

Non-invasive 2-D and 3-D bioluminescence imaging

4T1-FL2tDT orthotopic female CD1-nude mice were divided into control and treatment groups (n = 5 each) bearing large tumour (≥75 mm^3). The material control group received 180 μg/100 μL of Au-SLN, while the treatment group received the same amount of material, followed by 750 nm and 650 mW laser exposure for 4 minutes. For bioluminescence imaging, 3 mg D-luciferin in 100 μL 1× PBS was intraperitoneally administered. Under gas anaesthesia, 2D-BLI and 3D-BLI or DLIT were acquired in the IVIS Spectrum, Revvity. Analysis was performed using Living Image v4.4 software. The same acquisition and analysis procedure were followed for small-sized tumours (≤50 mm^3) at the early stage of growth. To achieve complete primary tumour ablation in large-sized tumour bearing female NOD-SCID mice (n = 3 for each control, NP and laser controls and PTT groups), multiple booster doses of PTT were given, and tumour progression was monitored by 2D-BLI.

Non-invasive 2-D and 3-D NIRF imaging

Female CD1-nude mice (n = 3) bearing ≥75 mm^3 orthotopic tumours before and after PTT were monitored using 2D-FLI and 3-D FLI (FLIT) NIRF imaging immediately after intravenous injection of 100 μL of XenoLight 2-DG-750 probe. The volumetric assessments of viable tumour as well as glucose probe uptake were analyzed using Living Image v4.4 software.

Statistical analysis

All *in vitro* and *in vivo* tests for comparison between treatment and control groups involved an unpaired t-test with Welsh correction and are represented as mean ± SEM. Sequential sum of squares was used to suggest a quadratic model for temperature response. ANOVA was applied to derive the fitness of the quadratic model for the temperature response. The Kaplan–Meier plot was used to analyse survival in animal experiments. A low cohort size was used to abide by the 3Rs (replacement, reduction and refinement) in animal research.

This journal is © The Royal Society of Chemistry 2025

Published on 06 Agosti 2025. Downloaded on 03/10/2025 02:20:03.

Author contributions

Conceptualization: A. De, R. Srivastava; funding acquisition: A. De; project administration: A. De, R. Srivastava; material resource: C. Patnaik, A. Ingle, P. Chaudhari, A. De; methodology: C. Patnaik, B. P. Reddy, A. Gupta, S. Asad, S. Rath, S. Neekhra, S. Chakrabarty, P. Chaudhari; investigation: C. Patnaik, A. Gupta, S. Rath, A. De; analysis: C. Patnaik, A. Gupta, S. Asad, S. Rath, A. Ingle, A. De; writing – original draft: C. Patnaik, B. P. Reddy, A. De; writing – review & editing: C. Patnaik, B. P. Reddy, A. Gupta, S. Rath, S. Neekhra, S. Chakrabarty, P. Chaudhari, S. Asad, A. Ingle, R. Srivastava, A. De.

Conflicts of interest

There are no conflicts to declare.

Data availability

The data supporting this article have been included as part of the SI.

Supplementary figures, tables and results have been provided in the SI file. See DOI: https://doi.org/10.1039/d5nr01472g.

Acknowledgements

We acknowledge TMC-ACTREC and DAE for intramural research funding to AD [Ref. DAE-ACTREC Grant No: 1/3(7)/2020/TMC/R&D-II/8823 Dt.30.07.2021]. PhD research fellowship by TMC-ACTREC to CP, SR, and AG and from IIT-B to BPR and SN is gratefully acknowledged. Institutional research infrastructure and various core facilities at ACTREC and IIT-B are also acknowledged.

References

1 N. Release and L. F. G. S. WHO, Global cancer burden growing, amidst mounting need for services, https://www.who.int/news/item/01-02-2024-global-cancer-burden-growing-amidst-mounting-need-for-services, (accessed 25 January 2025).
2 J. Ferlay, M. Colombet, I. Soerjomataram, C. Mathers, D. M. Parkin, M. Piñeros, A. Znaor and F. Bray, *Int. J. Cancer*, 2019, **144**, 1941–1953.
3 N. C. I. NIH, Types of Cancer Treatment, https://www.cancer.gov/about-cancer/treatment/types, (accessed 25 January 2025).
4 B. Liu, H. Zhou, L. Tan, K. T. H. Siu and X.-Y. Guan, *Signal Transduction Targeted Ther.*, 2024, **9**, 175.
5 E. S. Glazer and S. A. Curley, *Surg. Oncol. Clin. N. Am.*, 2011, **20**, 229–235.
6 M. Vats, S. K. Mishra, M. S. Baghini, D. S. Chauhan, R. Srivastava and A. De, *Int. J. Mol. Sci.*, 2017, **18**(5), 924.
7 S. K. Mishra, A. C. Dhadve, A. Mal, B. P. K. Reddy, A. Hole, M. K. Chilakapati, P. Ray, R. Srivastava and A. De, *Biomater. Adv.*, 2022, **143**, 213153.
8 W. Bian, Y. Wang, Z. Pan, N. Chen, X. Li, W.-L. Wong, X. Liu, Y. He, K. Zhang and Y.-J. Lu, *ACS Appl. Nano Mater.*, 2021, **4**, 11353–11385.
9 S. K. Mishra, A. Hole, B. P. K. Reddy, R. Srivastava, M. K. Chilakapati and A. De, *Nanomedicine*, 2021, **37**, 102437.
10 I. M. Mellal, E. K. Kengne, K. E. G. Guemhioui and A. L. Lakhssassi, *J. Biomed. Sci.*, 2016, **5**(4:28), DOI: 10.4172/2254-609X.100042.
11 P. Singh, S. Pandit, V. R. S. S. Mokkapati, A. Garg, V. Ravikumar and I. Mijakovic, *Int. J. Mol. Sci.*, 2018, **19**(7), 1979.
12 A. S. Abdoon, E. A. Al-Ashkar, O. M. Kandil, A. M. Shaban, H. M. Khaled, M. A. El Sayed, M. M. El Shaer, A. H. Shaalan, W. H. Eisa, A. A. G. Eldin, H. A. Hussein, M. R. El Ashkar, M. R. Ali and A. A. Shabaka, *Nanomedicine*, 2016, **12**, 2291–2297.
13 A. R. Rastinehad, H. Anastos, E. Wajswol, J. S. Winoker, J. P. Sfakianos, S. K. Doppalapudi, M. R. Carrick, C. J. Knauer, B. Taouli, S. C. Lewis, A. K. Tewari, J. A. Schwartz, S. E. Canfield, A. K. George, J. L. West and N. J. Halas, *Proc. Natl. Acad. Sci. U. S. A.*, 2019, **116**, 18590–18596.
14 L. Yang, Y. Zhang, J. Liu, X. Wang, L. Zhang and H. Wan, *Mater. Today Bio*, 2025, **31**, 101563.
15 C. Kong, B. Xu, G. Qiu, M. Wei, M. Zhang, S. Bao, J. Tang, L. Li and J. Liu, *Int. J. Nanomed.*, 2022, **17**, 5391–5411.
16 M. Wang, Y. Li, M. Wang, K. Liu, A. R. Hoover, M. Li, R. A. Towner, P. Mukherjee, F. Zhou, J. Qu and W. R. Chen, *Acta Biomater.*, 2022, **138**, 453–462.
17 B. P. K. Reddy, S. K. Mishra, G. Ravichandran, D. S. Chauhan, R. Srivastava and A. De, *Appl. Mater. Today*, 2020, **20**, 100684.
18 J. B. Vines, J.-H. Yoon, N.-E. Ryu, D.-J. Lim and H. Park, *Front. Chem.*, 2019, **7**, DOI: 10.3389/fchem.2019.00167.
19 M. A. El-Sayed, *Acc. Chem. Res.*, 2001, **34**, 257–264.
20 Z. Weiszhár, J. Czúcz, C. Révész, L. Rosivall, J. Szebeni and Z. Rozsnyay, *Eur. J. Pharm. Sci.*, 2012, **45**, 492–498.
21 N. Raval, R. Maheshwari, D. Kalyane, S. R. Youngren-Ortiz, M. B. Chougule and R. K. Tekade, in *Basic Fundamentals of Drug Delivery*, Elsevier, 2019, pp. 369–400.
22 D. S. Chauhan, A. B. Bukhari, G. Ravichandran, R. Gupta, L. George, R. Poojari, A. Ingle, A. K. Rengan, A. Shanavas, R. Srivastava and A. De, *Sci. Rep.*, 2018, **8**, 16673.
23 K. Laxman, B. P. K. Reddy, S. K. Mishra, M. B. Gopal, A. Robinson, A. De, R. Srivastava and M. Ravikanth, *ACS Appl. Mater. Interfaces*, 2020, **12**, 52329–52342.
24 K. Laxman, B. P. K. Reddy, S. K. Mishra, A. Robinson, A. De, R. Srivastava and M. Ravikanth, *NPG Asia Mater.*, 2020, **12**, 75.
25 A. Shetty, S. K. Mishra, A. De and S. Chandra, *J. Drug Delivery Sci. Technol.*, 2022, **70**, 103252.

Published on 06 Agosti 2025. Downloaded on 03/10/2025 02:20:03.

26 B. Singh, C. Patnaik, R. Bahadur, M. Gandhi, A. De and R. Srivastava, *Nanoscale*, 2023, **15**, 1273–1288.
27 D. S. Chauhan, P. Arunkumar, R. Prasad, S. K. Mishra, B. P. K. Reddy, A. De and R. Srivastava, *Mater. Sci. Eng., C*, 2018, **90**, 539–548.
28 D. S. Chauhan, M. K. Kumawat, R. Prasad, P. K. Reddy, M. Dhanka, S. K. Mishra, R. Bahadur, S. Neekhra, A. De and R. Srivastava, *Colloids Surf., B*, 2018, **172**, 430–439.
29 C. Schwarz and W. Mehnert, *Int. J. Pharm.*, 1997, **157**, 171–179.
30 E. Trenkenschuh and W. Friess, *Eur. J. Pharm. Biopharm.*, 2021, **165**, 345–360.
31 M. Fenech, *Nat. Protoc.*, 2007, **2**, 1084–1104.
32 E. P. Rogakou, C. Boon, C. Redon and W. M. Bonner, *J. Cell Biol.*, 1999, **146**, 905–916.
33 S. Yedgar, G. Barshtein and A. Gural, *Micromachines*, 2022, **13**, 2091.
34 Cleveland Clinic, Burns, **https://my.clevelandclinic.org/health/diseases/12063-burns**, (accessed 18 February 2025).
35 M. P. Rowan, L. C. Cancio, E. A. Elster, D. M. Burmeister, L. F. Rose, S. Natesan, R. K. Chan, R. J. Christy and K. K. Chung, *Crit. Care*, 2015, **19**, 243.
36 L. Li, C. Chen, H. Liu, C. Fu, L. Tan, S. Wang, S. Fu, X. Liu, X. Meng and H. Liu, *Adv. Funct. Mater.*, 2016, **26**, 4252–4261.
37 Y. Tian, R. Guo and W. Yang, *Adv. Ther.*, 2018, **1**(8), DOI: **10.1002/adtp.201800049**.
38 L. Lei, P. Liu, W. Jing and Z. Wu, *Nano TransMed*, 2023, **2**, 100022.
39 D. S. Chauhan, B. P. K. Reddy, S. K. Mishra, R. Prasad, M. Dhanka, M. Vats, G. Ravichandran, D. Poojari, O. Mhatre, A. De and R. Srivastava, *Langmuir*, 2019, **35**, 7805–7815.
40 R. G. Chaudhuri and S. Paria, in *Kirk-Othmer Encyclopedia of Chemical Technology*, Wiley, 2013, pp. 1–44.
41 X. Liu, B. Li, F. Fu, K. Xu, R. Zou, Q. Wang, B. Zhang, Z. Chen and J. Hu, *Dalton Trans.*, 2014, **43**, 11709.

This journal is © The Royal Society of Chemistry 2025